remote sensing

MDPI

Article

Retrieval of Vertical Cloud Droplet Profiles and Above-Cloud Integrated Water Vapor from Hyperspectral Measurements: Reducing Liquid Water Path Retrieval Bias with Application to EMIT

Andrew John Buggee [1,2,*] and Peter Pilewskie [1,2]

[1] Laboratory for Atmospheric and Space Physics, University of Colorado Boulder, Boulder, CO 80303, USA; peter.pilewskie@lasp.colorado.edu
[2] Department of Atmospheric and Oceanic Sciences, University of Colorado Boulder, Boulder, CO 80303, USA
* Correspondence: andrew.buggee@lasp.colorado.edu

Highlights

What are the main findings?

- A Gauss–Newton optimal estimation retrieval simultaneously retrieves vertical profiles of cloud droplet effective radius, cloud optical thickness, and above-cloud integrated water vapor from hyperspectral solar backscatter measurements, reducing liquid water path bias from 45% (standard bispectral method) to 27% against in situ measurements.
- Application to 3695 EMIT pixels over the southeast Pacific shows that MODIS liquid water path retrievals, which assume a vertically homogeneous cloud, exceed the hyperspectral estimate by 19% on average, consistent with the expected bias direction from prior comparisons with retrievals using microwave observations.

What are the implications of the main findings?

- Simultaneous retrieval of integrated water vapor above-cloud improves the accuracy of droplet profile retrievals: assuming a fixed water vapor column introduces biases in retrieved effective radius at cloud top and base.
- Measurements from the HySICS instrument on CLARREO Pathfinder, with contiguous spectral sampling at 636 wavelengths between 350 nm and 2300 nm with 0.3% radiometric uncertainty, are expected to enable routine, accurate retrievals of vertical cloud droplet profiles, improving the estimates of cloud liquid water path compared to traditional bispectral methods.

Abstract

Accurate liquid water path estimates derived from backscattered solar radiation require knowledge of the vertical structure of cloud droplet effective radius, yet standard bispectral retrievals assume a vertically homogeneous cloud and overestimate liquid water path by up to 45% compared to in situ measurements. We developed a Gauss–Newton optimal estimation retrieval that simultaneously estimates vertical profiles of cloud droplet effective radius, cloud optical thickness, and above-cloud integrated water vapor from hyperspectral solar backscatter measurements in the visible and shortwave infrared. The retrieval solves for effective radius at cloud top and base, cloud optical thickness, and above-cloud integrated water vapor in logarithmic space, using an a priori covariance matrix with off-diagonal elements derived from VOCALS-REx in situ measurements, and incorporating forward model uncertainty with a forward model Jacobian. Tested on 69 simulated

Check for updates

Academic Editor: Filomena Romano

Received: 26 March 2026
Revised: 24 July 2026
Accepted: 24 July 2026
Published: 3 August 2026

Copyright: © 2026 by the authors. Licensee MDPI, Basel, Switzerland. This article is an open access article distributed under the terms and conditions of the Creative Commons Attribution (CC BY) license.

HySICS reflectance spectra constructed from in situ cloud microphysics, the hyperspectral retrieval reduces the average liquid water path error to 26.9%, compared to 45.2% for the standard bispectral method. Applied to 3695 EMIT hyperspectral measurements over the southeast Pacific, MODIS-retrieved liquid water path exceeds the hyperspectral estimate by 19% on average. These results demonstrate that simultaneous retrieval of the integrated water vapor above-cloud is necessary for accurate droplet profile retrievals, and that the upcoming CLARREO Pathfinder instrument, with its 0.3% radiometric uncertainty, should enable routine vertical profiling of cloud droplet size.

Keywords: cloud remote sensing; retrievals; hyperspectral measurements; cloud optical properties

1. Introduction

Marine stratus and stratocumulus clouds cover approximately 12% and 23% of the global ocean surface on the annual mean, respectively, and occur most frequently over cold eastern ocean basins [1]. These clouds typically form in the boundary layer and are strong reflectors of incident solar radiation, with an average top-of-atmosphere cooling effect of $-1.4\ \mathrm{W/m^2}$ and $-8.3\ \mathrm{W/m^2}$, respectively [2]. The abundance and cooling effect of marine stratus and stratocumulus make them vital to our understanding of Earth's radiative energy balance [3].

Theoretical models of warm, non-precipitating adiabatic clouds predict a vertical structure of droplet size that increases from cloud base to cloud top, with many in situ measurements verifying this prediction [4–6]. Vertical profiles of cloud droplet size can be used to determine the droplet growth process and the mixing of cloud top with dry air above [7–9]. In addition, vertical droplet profiles are required for an accurate estimation of liquid water path, the vertically integrated water content, and cloud albedo [10–12].

For many decades, space-borne spectrally resolved measurements of reflected solar radiation over cloudy scenes have been used to remotely determine cloud droplet effective radius, defined as the ratio of the third moment to the second moment of the droplet size distribution, and cloud optical thickness, the number of photon mean free paths [13]. Twomey and Seton [14] outlined what is now considered the standard method for deriving cloud optical properties with spectral measurements in the visible (0.4 μm to 0.7 μm) and shortwave infrared (1 μm to 2.5 μm for this study). This optical remote sensing method, often referred to as the two-band lookup table method (TBLUT), can be applied to measured reflectance in as few as two spectral bands: one at a wavelength where absorption by water is negligible and the other at a wavelength where water weakly absorbs [14–16]. A decades long record of effective radius and optical depth derived using the TBLUT method now exists and has been used to glean climatological information on clouds [17]. However, the TBLUT method derives a column-weighted average of the actual vertical droplet size profile [18]. Retrieving a column-weighted average, which neglects the vertical variation in droplet size, is one reason that the TBLUT method was found to overestimate liquid water path by as much as 25% [12,17].

Due to the variability of absorption by liquid water in the shortwave infrared, this results in a wavelength-dependent effective radius. This was explained by Platnick [19], who showed that photons at different wavelengths penetrate to different depths within clouds due to the spectral dependence of droplet single scattering albedo. Thus, the retrieved droplet radius represents a weighted average over the vertical extent of the cloud, with the largest weighting occurring near cloud top [19]. This wavelength dependence

laid the foundation for using measurements at multiple shortwave infrared wavelengths to retrieve vertical profiles of droplet size that capture vertical variation [20–24].

Following Platnick [19], Chang and Li [21] proposed using Moderate Resolution Imaging Spectroradiometer (MODIS) measurements at three shortwave infrared spectral bands to retrieve the vertical dependence of effective droplet radius. Their method assumed a linear relationship between effective droplet radius and altitude within the cloud. In another study, Kokhanovsky and Rozanov [22] outlined a mathematical framework for applying the Gauss–Newton optimal estimation (GNOE) technique to infer a vertical droplet profile using spectral measurements. They showed that MODIS measurements at four different shortwave infrared wavelengths could be used simultaneously with less computational cost than the lookup table method to solve for three variables: the effective radii at cloud top and cloud base (the geometric levels associated with an optical depth of zero and the full cloud optical thickness, respectively), and cloud optical thickness, demonstrating their method with synthetic and real MODIS measurements. King and Vaughan [23] applied an optimal estimation technique to synthetic spectral reflectance throughout the visible and shortwave infrared to retrieve effective radii at cloud top and base, cloud optical thickness and the integrated water vapor content above cloud. Buggee and Pilewskie [20] built on these results by developing an optimal estimation retrieval method to estimate vertical droplet profiles from MODIS measurements coincident with in situ data for comparison, the first of its kind. They determined that the uniqueness of the retrieved droplet profile is predominantly impacted by the measurement and forward model uncertainty, and to a lesser degree, the number of spectral channels used. See Buggee and Pilewskie [20] for a thorough description of these previous studies.

Hyperspectral sensors that sample the solar spectrum in many hundreds of contiguous spectral bands have been proposed and built, with some already launched and others soon to be [25–28]. Coddington et al. [29] and King and Vaughan [23] have shown that these measurements contain a wealth of information on cloud properties. The increase in spectral sampling, which enables different vertical sampling levels within a cloud, and the reduction in radiometric uncertainty, which reduces solution non-uniqueness, of upcoming space-borne hyperspectral imaging spectrometers can be leveraged to routinely retrieve vertical cloud droplet profiles, rather than a single column-weighted average, enhancing our understanding of cloud droplet growth, cloud–aerosol interactions, and cloud albedo.

The Calibration Absolute Radiance and Refractivity Earth Observatory (CLARREO) Pathfinder (CPF) is an upcoming space-borne hyperspectral imaging spectrometer that will soon deploy on the International Space Station (ISS) with a near-circular orbit and an average altitude of 417 km and an inclination of 51.6° [28]. The full CPF swath width is 70 km, comprised of 480 cross-track pixels [28]. The CPF Hyperspectral Imager for Calibration Science (HySICS) is the most radiometrically accurate space-borne hyperspectral imager ever built for Earth science, with a radiometric uncertainty of 0.3% [28]. HySICS will measure scattered radiation contiguously from 350 nm to 2300 nm with a spectral resolution of 6 nm and Nyquist sampling [30]. With an instantaneous field of view of 0.02°, HySICS will have a spatial sampling of about 0.5 km at nadir after three-pixel binning.

In this paper, we expanded on the vertical droplet profile retrieval method of Buggee and Pilewskie [20] to utilize the enhanced radiometric accuracy and spectral resolution of CPF and applied it to real hyperspectral measurements for the first time. The research herein builds upon previous studies in several ways. First, we build on the results of King and Vaughan [23] and show that retrieving the integrated water vapor content above cloud improves the accuracy of the retrieved droplet profile. Second, all previous studies attempting to retrieve a droplet profile using optimal estimation methods assumed the retrieved variables were uncorrelated [20,22,23]. This is not the best representation of

the true physics of the problem. In this study, we used in situ measurements from the Variability of the American Monsoon Systems Ocean–Cloud–Atmosphere–Land Study Regional Experiment (VOCALS-REx) field campaign to compute the a priori covariance matrix, including the off-diagonal elements [31]. Third, previous studies showed the importance of transforming the optimal estimation framework into logarithmic space when the retrieved variables more closely follow lognormal distributions [32,33]. We show that the effective radii at cloud top and base, the cloud optical thickness and the integrated water vapor content above cloud follow log-normal distributions more closely than normal distributions, warranting this transformation. Lastly, a study of forward model uncertainty was undertaken in order to understand each component's impact on retrieval performance. The droplet profile retrieval was then tested on real hyperspectral measurements from the Earth Surface Mineral Dust Source Investigation (EMIT) imaging spectrometer [34] and compared against retrievals using measurements from the instruments onboard the Aqua satellite, the first such retrieval and comparison of its kind. With a similar spectral range, albeit coarser spectral resolution, the EMIT instrument acts as a surrogate for the upcoming CPF instrument.

Section 2 provides background information on previous studies, describes the details of the optimal estimation retrieval method, and the construction of simulated HySICS reflectance. Section 2 also describes the selection of EMIT measurements with spatially and temporally coincident observations from instruments onboard the Aqua satellite, along with modifications to the retrieval method for application to real hyperspectral data. Section 3 presents results from applying our retrieval to simulated HySICS reflectance, demonstrating the importance of simultaneously retrieving above-cloud integrated water vapor and quantifying retrieval performance using in situ-defined cloud profiles. Section 3 also presents results from applying our retrieval to EMIT measurements, with comparisons to coincident satellite observations. Section 4 provides a discussion of the results and concluding remarks on the utility of hyperspectral measurements for retrieving vertical cloud structure and above-cloud integrated water vapor.

2. Background, Data, and Methods

2.1. Retrieval Methodology

We built on the Gauss–Newton iterative retrieval algorithm developed by Buggee and Pilewskie [20], an optimal estimation method grounded in Bayesian probability [35]. This approach combines prior information about retrieved variables with spectral measurements, each weighted by their respective uncertainties through covariance matrices. With every iteration, the algorithm updates the state vector by balancing the difference between calculated and true reflectance against deviations from the prior. For the complete mathematical formulation, see Buggee and Pilewskie [20].

At each iteration, a new state vector, $\boldsymbol{x}_{i+1} = \left(\boldsymbol{r}_{top}, \boldsymbol{r}_{bot}, \boldsymbol{\tau}_c, \boldsymbol{IWV}_{ac}\right)$, is estimated:

$$\boldsymbol{x}_{i+1} = \boldsymbol{x}_i + \left(\mathbf{S}_a^{-1} + \mathbf{K}_i^T \mathbf{S}_\epsilon^{-1} \mathbf{K}_i\right)^{-1} \left[\mathbf{K}_i^T \mathbf{S}_\epsilon^{-1} (\boldsymbol{m} - \boldsymbol{R}(\boldsymbol{x}_i)) + \mathbf{S}_a^{-1} (\boldsymbol{x}_i - \boldsymbol{x}_a)\right] \quad (1)$$

where matrices are indicated in capitalized boldface, and vectors are indicated in lowercase boldface. $\boldsymbol{x_i}$ is the state vector estimate of the $\boldsymbol{i}$–th iteration, $\boldsymbol{x_a}$ is the a priori state vector, $\boldsymbol{S_a}$ is the a priori covariance matrix, $\boldsymbol{K_i}$ is the Jacobian of the forward model $\boldsymbol{R}(\boldsymbol{x_i})$, and $\boldsymbol{S_\epsilon}$ is the effective measurement covariance matrix. The state vector, $\boldsymbol{x} = \left(\boldsymbol{r}_{top}, \boldsymbol{r}_{bot}, \boldsymbol{\tau}_c, \boldsymbol{IWV}_{ac}\right)$, represents the effective radii at cloud top and base, the cloud optical thickness, and the integrated water vapor content above cloud, respectively. The effective measurement covariance matrix combines measurement and forward model uncertainties: $\boldsymbol{S_\epsilon} = \boldsymbol{S_m} + \boldsymbol{S_{fm}^{'}}$ [36]. $\boldsymbol{S_m}$ defines the measurement uncertainty at each wavelength and the correlation between

measurements at different wavelengths. $S_{fm}^{'}$ defines the forward model uncertainty in measurement space. The forward model, $\boldsymbol{R}$, computes reflectance at a set of wavelengths for a given cloud state, $\boldsymbol{x_i}$. The Jacobian represents the change in reflectance resulting from a perturbation in each state variable. Equation (1) balances several competing factors during each iteration: the difference between measured and computed reflectance $(\boldsymbol{m} - \boldsymbol{R}(\boldsymbol{x_i}))$, the difference between the current state estimate and the a priori $(\boldsymbol{x_i} - \boldsymbol{x_a})$, and the rate of change in the estimated measurements with respect to the current state variable $\mathbf{K_i} = \nabla \boldsymbol{R}(\boldsymbol{x_i})$.

We use the two convergence criteria from [20], with the cost function defined as the root-sum-square of the difference between the forward model reflectance and the true measurements. Convergence is satisfied in two ways: (1) the percent difference of the cost function between two successive iterations falls below 3%, or (2) the cost function becomes less than or equal to the root-sum-square of the total uncertainty (measurement and forward model), and is lower than the previous iteration [20,37]. Once convergence occurs, the posterior covariance matrix is computed (see Equation (13) in [20]). The uncertainties of the retrieved variables are the square root of the main diagonal [35]. It is important to note that this method does not find the global minimum, but rather a local minimum that depends strongly on the prior information and initial guess [33]. Lastly, our retrieval enforced the physical constraint that the effective radius at cloud top exceeds that at cloud base [20], following [37]. This constrained form of GNOE reduced the number of iterations required, resulting in rapid convergence. This reflects the constrained solver framework rather than negligible contributions from measurements.

2.2. Simulated HySICS Reflectance and Forward Model Assumptions

Before applying our algorithm to real data, we tested our method on simulated HySICS reflectance to quantify retrieval accuracy when the forward model and radiometric uncertainty were precisely known. Reflectance was computed in a manner similar to the synthetic data generated by King and Vaughan [23]. Cloud droplet profiles were modeled as smooth, monotonic, and adiabatic following Platnick [19], with 20 plane-parallel cloud layers, each with a gamma droplet distribution. The effective variance, which defines the width and asymmetry of the distribution, was defined as the column-average of the in situ measurements from the VOCALS-REx field campaign. We note that the assumption of a vertically constant effective variance is a simplification that is not valid for all clouds, and that in situ measurements have found that droplet distributions often narrow towards cloud top [5].

libRadtran was used to compute top-of-atmosphere reflected radiance by using 1-D DISORT to solve the equation of radiative transfer [38,39]. Reflectance from 350 nm to 2300 nm at the HySICS sampling resolution of 3 nm was estimated by convolving the radiance spectrum with the HySICS slit functions and normalizing by the incident solar irradiance. The TSIS-1 hybrid solar reference spectrum was used [40]. We assumed a uniform radiometric uncertainty of 0.3% across all spectral channels [28]. This dataset was used to isolate the effect of an incorrect forward model assumption on the amount of above-cloud integrated water vapor on retrieval performance in the absence of other forward model uncertainties (Section 3.1).

Next, a second HySICS reflectance dataset was generated using VOCALS-REx in situ measurements to simulate more realistic clouds [31]. Sixty-nine in situ vertical profiles of non-precipitating clouds where a C-130 aircraft sampled the droplet distribution between cloud base and top were identified. This dataset will be referred to as the in situ measured profiles for the remainder of the paper. Reflectance spectra were computed from these profiles by defining each cloud using the in situ measured cloud boundaries (base and

top) and droplet size distribution, and the in situ derived cloud optical thickness. We used definitions similar to [6], defining cloud top and base with a minimum liquid water content of 0.03 g/m^3 and a minimum total droplet number concentration threshold of 25 cm^{-3}. Therefore, cloud top and base were identified as the maximum and minimum altitudes where both criteria were satisfied.

For each in situ measured profile, the above cloud integrated water vapor content was defined using data from the European Centre for Medium-Range Weather Forecasts (ECMWF) Reanalysis version 5 (ERA5) [41]. ERA5 combines historical observations from satellites, weather stations, and other sources with numerical weather prediction models through data assimilation to create a spatially and temporally complete, physically consistent reconstruction of the Earth's atmosphere from 1940 to present [41]. Above-cloud integrated water vapor was defined by integrating ERA5 water vapor concentration from the VOCALS-REx in situ measured cloud top altitude to the top of the atmosphere. For each in situ measured profile, we found the ERA5 dataset closest in time and space. We note that the use of radiosonde data, which was extensive throughout the VOCALS-REx field campaign, was explored. However, the average spatial distance and time difference between the in situ measured profiles and the closest radiosonde measurement were 735 km and 63 min, respectively, whereas for ERA5 data these values were 9 km and 14 min, respectively. Often the same radiosonde profile was found to be the closest in time and space for several in situ measured profiles, leading to redundant $\boldsymbol{IWV_{ac}}$ measurements. The choice between radiosonde and ERA5 data significantly impacted the a priori covariance matrix (see Section 2.5). Radiosonde measurements of above-cloud integrated water vapor averaged four times higher than corresponding ERA5 estimates for the same in situ profiles, which may be due to the large spatial and temporal offsets between the radiosonde and in situ measurements.

Our analysis was restricted to non-precipitating marine clouds over the ocean with a cloud optical thickness of at least three. The optical depth threshold was chosen to avoid the non-uniqueness of effective radius retrievals for optically thin clouds [15]. We adopted some assumptions from the forward model used in the MODIS Collection 6 cloud optical properties retrieval algorithm. These included assuming maritime aerosols with an aerosol optical depth of 0.1 and using the Cox–Munk surface bidirectional reflectance model to account for the impact on reflectance over the ocean with a particular wind speed and direction [18,42]. We used the US standard atmosphere to define vertical profiles of all atmospheric gases other than water vapor [43]. Lastly, reflectance at one wavelength was assumed to be independent of reflectance at every other wavelength, resulting in a diagonal measurement covariance matrix, $\boldsymbol{S_m}$, where each element along the main diagonal was defined as the square of the reflectance uncertainty at that wavelength. A diagonal covariance matrix does not reflect the true nature of the instrument, but it is a common simplifying assumption [22,23,36].

2.3. Retrieval of Above-Cloud Integrated Water Vapor Content

Historically, space-borne spectral measurements used to infer cloud properties sampled regions of reflected solar radiation where water vapor weakly absorbs [44–46]. The advantage of avoiding spectral regions with appreciable absorption by water vapor is that accurate knowledge of the column water vapor amount is not crucial. However, absorption by water vapor is ubiquitous, with many weak to strong lines spanning the solar spectrum. King and Vaughan [23] showed there was additional information content in the wings of water vapor absorption bands that could be leveraged to improve the estimate of droplet size near cloud top. To leverage the full spectrum of CPF for the retrieval of a droplet profile, the above-cloud integrated water vapor content needs to be retrieved simultaneously.

Figure 1 shows a set of weighting functions, a conditional probability that a photon scattering in the upward direction at cloud top penetrated to some maximum optical depth, τ, within a cloud with optical thickness τ_c. The weighting functions in Figure 1 were derived from radiative transfer calculations using the HySICS slit functions following the method of Platnick [19]. Figure 1 demonstrates the importance of including measurements in the wings of water vapor absorption regions for droplet profile retrievals. The selection of wavelengths, shown in the figure legend, was chosen to emphasize a spread in the peak value. The set of weighting functions shown in Figure 1 demonstrates a larger degree of relative orthogonality than a set that does not sample the wings of water vapor absorption features (compare with Figure 1 from Buggee and Pilewskie [20]). The average penetration depth of reflected photons shifts toward cloud top for wavelengths close to a strong water vapor absorption band, whereas photons at wavelengths with little water vapor and liquid water absorption have average penetration depths further into the cloud.

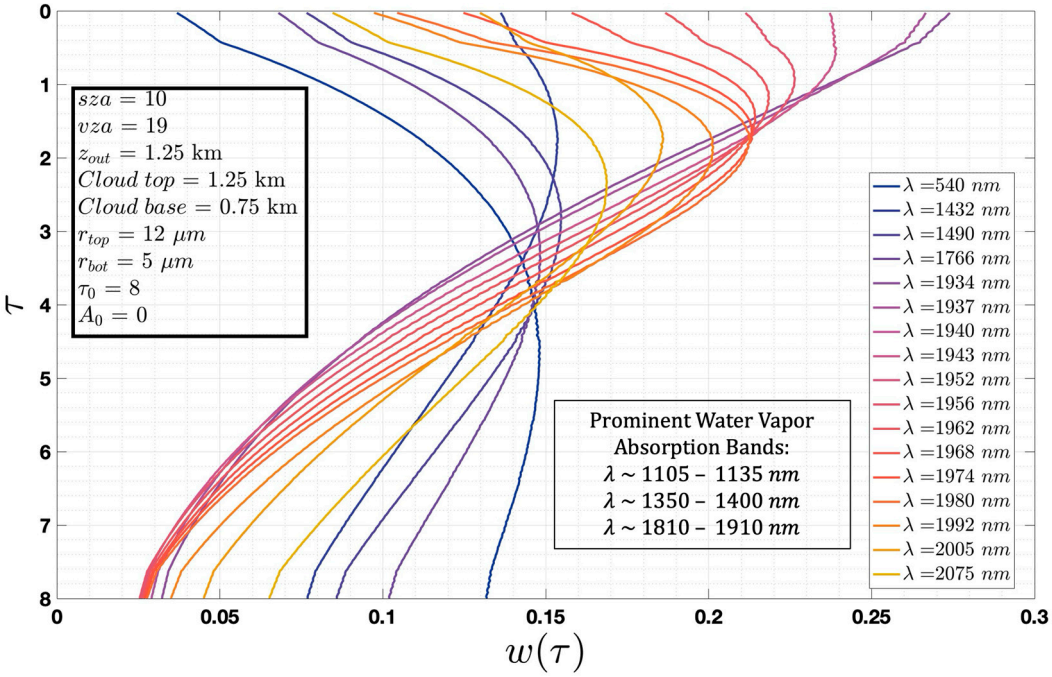


Figure 1. A set of weighting functions derived from simulated HySICS reflectance. The center wavelength of each spectral channel is listed in the legend. The text box on the left describes the solar and viewing zenith angles, the cloud top and base height, the effective radii at cloud top and base, the cloud optical thickness and the surface albedo. Several prominent water vapor absorption bands are defined in the text box on the right-hand side.

This physical basis for retrieving integrated water vapor content above cloud from backscattered light was outlined by Albert et al. [47], who showed that marine stratus and stratocumulus have two opposing contributions to the total absorption by water vapor. The lowest layers of the atmosphere, where most of the water vapor resides, do not contribute to the reflected signal, thus lessening the total absorption (this effect is less prominent for optically thin clouds). On the other hand, multiple scattering within the cloud increases the total radiation absorbed by increasing the path length photons travel. Albert et al. [47] computed vertical weighting functions to determine the contribution of different cloud layers to the total absorption by water vapor and found that the total absorption for optically thick clouds over ocean was primarily due to the above-cloud integrated water vapor content.

To retrieve IWV_{ac} simultaneously alongside r_{top}, r_{bot}, and τ_c, an initial guess at the true value is required. Thus, we developed a multi-spectral method for estimating IWV_{ac}

based on the differential absorption method of Albert et al. [47]. First, we estimated the effective radius and cloud optical thickness using a multi-spectral TBLUT retrieval method based on the algorithm described by Amarasinghe et al. [18]. Using these results, IWV_{ac} was estimated using a lookup table of computed reflectance at 900 nm, 955 nm, and 1127 nm for IWV_{ac} values between 0 and 40 mm. The bulk absorption coefficient of water vapor varies at these three wavelengths, leading to regions that absorb different amounts of incident radiation. The solution was determined by solving for the minimum root–sum–square between the look-up table and the simulated HySICS reflectance. This multi-spectral estimate was subsequently used as the initial guess in the GNOE retrieval of IWV_{ac}.

2.4. Transforming the Gauss–Newton Formalism into Log-Space

A core assumption of the Gauss–Newton iterative method is that the prior and measurement uncertainties follow a normal distribution [48]. Previous work has shown that the distribution of many positively defined atmospheric variables more closely follows a log-normal distribution [32,33]. Maahn et al. [33] showed that transforming the GNOE framework into log-space when the variables of interest more closely follow a log-normal distribution resulted in an increased convergence rate from 86% to 100%.

To determine whether the retrieved variables better fit a normal or log-normal distribution, we created an a priori dataset using VOCALS-REx in situ measurements to define r_{top}, r_{bot}, and τ_c, and ERA5 reanalysis data to define IWV_{ac}. r_{top} and r_{bot} were defined as the average effective radius over the top and bottom 25% of each in situ measured vertical profile with respect to the normalized altitude within cloud in order to average over rapid vertical fluctuations in $r_e(z)$. Cloud optical thickness was determined from the in situ measurement of the droplet size distribution: $\tau_c^{\lambda} = \int\int \sigma_e^{\lambda}(r) n(r,z) dr dz$, where σ_e^{λ} is the spectral extinction cross section of liquid water, and $n(r,z)$ is the droplet size distribution. For this study, τ_c was computed at $\lambda = 500$ nm. The integrated water vapor content was derived from ERA5 data as the integral of water vapor concentration from the in situ measured cloud top height to the top of the atmosphere.

Figure 2a,b show quantile–quantile plots for all four retrieved variables, with an R^2 value to indicate how well each variable fits a normal (panel a) and log-normal (panel b) distribution. All four variables have a higher R^2 value in panel (b), indicating that they more closely follow a log-normal distribution. Therefore, we made the following transformations to the measurement and state vectors:

$$m' = \ln(m), \quad x_a' = \ln(x_a), \quad x_i' = \ln(x_i) \tag{2}$$

The measurement and prior covariance matrices are transformed into log space by taking the log of the prior dataset and the measurements:

$$\begin{aligned} S_a' &= \mathbf{Cov}\left(\ln\left(\left[r_{top}, r_{bot}, \tau_c, IWV_{ac}\right]\right)\right) \\ S_\epsilon' &= \mathbf{Cov}\left(\ln\left(\left[m_{\lambda_1}, m_{\lambda_2}, \ldots, m_{\lambda_M}\right]\right)\right) \end{aligned} \tag{3}$$

We compute the Jacobian in log-space as follows [49]:

$$K' = \frac{\partial m'}{\partial x'} = \frac{\partial m}{\partial x}\frac{x}{m} = K\frac{x}{m} \tag{4}$$

Reformulating Equation (1) into log space, we solve for the logarithm of the state vector at each iteration:

$$x_{i+1}' = x_i' + \left(S_a'^{-1} + K_i'^{T} S_\epsilon'^{-1} K_i'\right)^{-1}\left[K_i'^{T} S_\epsilon'^{-1}\left(m' - R\left(x_i'\right)\right) + S_a'^{-1}\left(x_i' - x_a'\right)\right] \tag{5}$$

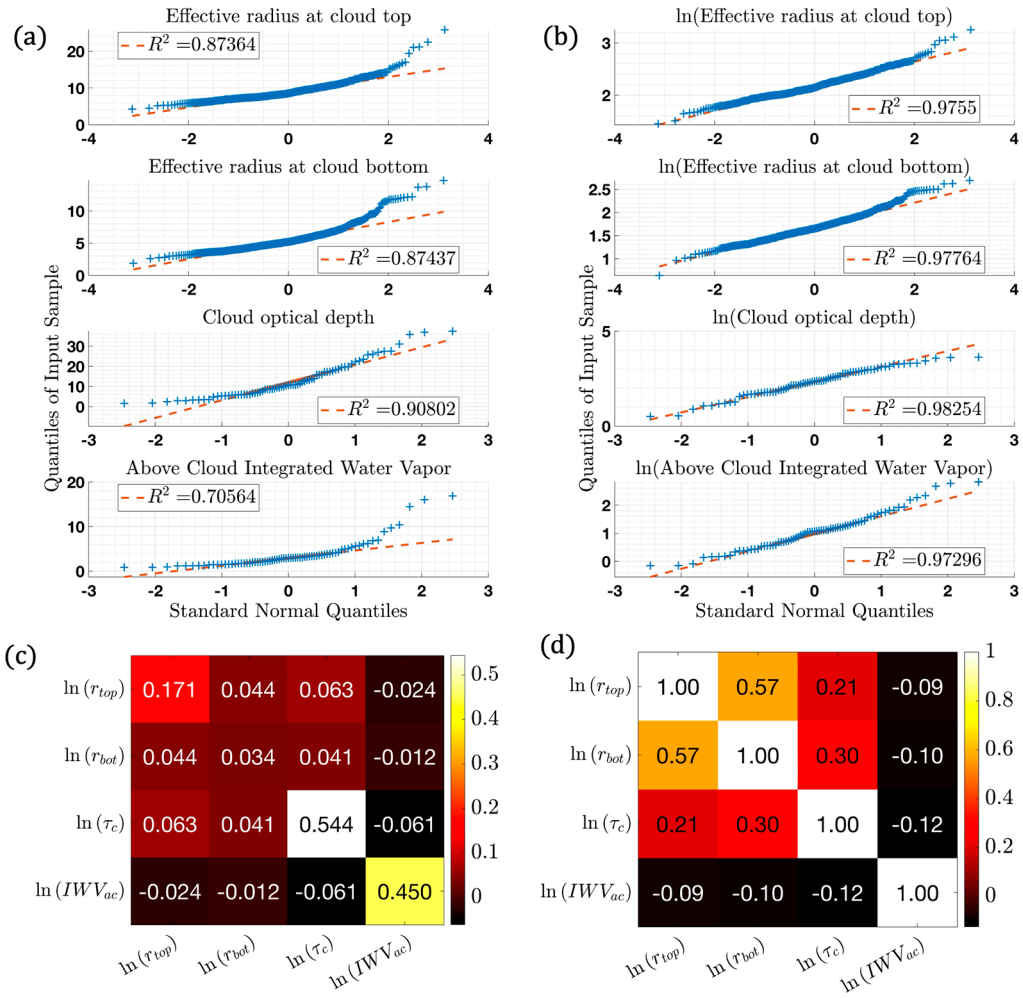


Figure 2. Panel (**a**) shows the quantile–quantile plot for all four retrieved variables. Panel (**b**) shows the same but for the natural logarithm of each variable. The R^2 value is listed for each quantile–quantile plot, where a value of 1 indicates a perfect fit. Panel (**c**) shows the a priori covariance matrix in log space (Equation (3)). Panel (**d**) shows the correlation coefficients of the a priori covariance matrix.

2.5. Computation of the a Priori Covariance Matrix

In the Gauss–Newton formulation, the prior is defined by a Gaussian distribution with mean, $\boldsymbol{x_a}$, and covariance, $\boldsymbol{S_a}$ [35]. At each iteration, the difference between the current guess and the prior is computed. Solutions far from the prior are penalized. If the true value is not well represented by the prior, the result is likely to be inaccurate [33]. We used the a priori dataset described in Section 2.4 to determine the a priori covariance matrix.

Figure 2c shows the resulting matrix in log space. Values along the main diagonal show the variance of the effective radii at cloud top and base, the cloud optical thickness, and the above-cloud integrated water vapor, respectively. The off-diagonal elements show the covariance between variables. To better interpret the results, Figure 2d shows the correlation coefficient matrix, the covariance matrix normalized by the variance. Values in this matrix are often referred to as the Pearson correlation, with $\boldsymbol{r} = {}^{Cov(X,Y)}/_{\sigma_Y \sigma_X}$ where σ_X is the standard deviation of the random variable $\boldsymbol{X}$ [50]. Values range from $[-1, 1]$, implying a strong negative linear relationship and a strong positive linear relationship, respectively. The square of the Pearson correlation, sometimes called the coefficient of determination, defines the proportion of variance in one variable that can be explained by the linear relationship with the other [50].

The effective radii at cloud top and base have the strongest positive Pearson correlation of 0.57 and a coefficient of determination of 0.325. This suggests some vertical coherence between the droplet size at cloud top and base, such as a quasi-adiabatic structure. However, with only 32.5% of the variance in r_{top} explained by r_{bot} (and vice versa), decoupling processes, such as cloud top entrainment, likely break down this coherence. The Pearson correlations between cloud optical thickness and effective radii at cloud top and base are 0.21 and 0.3, with coefficients of determination of 0.044 and 0.09, respectively. Interestingly, all Pearson correlations with integrated water vapor above cloud were negative and of small magnitude.

Several caveats should be mentioned with regard to the correlation coefficient matrix. A bias may exist due to the different data sources used to estimate these variables: r_{top}, r_{bot}, and τ_c were defined using measurements from a Cloud Droplet Probe (CDP) [51], whereas ERA5 reanalysis data were used to define IWV_{ac}. In addition, with only 69 in situ measured droplet profiles, these correlations may suffer from an under sampling of the full distribution of each variable. Lastly, there are spatial and temporal differences between the CDP measurements and ERA5 reanalysis data that may be behind some of the results. The mechanisms behind the relationships described above require further investigation with larger in situ datasets before any confident conclusions can be reached.

2.6. Forward Model Uncertainty and Jacobian

Forward model uncertainty is often ignored despite having an impact on retrieval uncertainty [35]. Indeed, with HySICS radiometric uncertainty being only 0.3%, retrieval uncertainty is likely limited by forward model uncertainty. Several forward model assumptions that represent some of the largest sources of uncertainty according to previous studies are as follows: cloud top height uncertainty, deviations from the assumed smooth, monotonic adiabatic profile, and uncertainty in effective variance of the droplet size distribution [36,52].

For all retrievals using synthetic HySICS reflectance, the cloud top height was assumed to be the mean value from the a priori dataset (Section 2.5) of 1.2 km, and the uncertainty was defined as the a priori standard deviation of 0.218 km. Forward model uncertainty due to the assumption of a smooth, monotonic adiabatic droplet profile exists because of the difference between the calculated reflectance from the retrieved profile and the measured reflectance that results from the true profile. The forward model used 20 plane-parallel layers to define clouds with vertical variation. For each layer, the mean and standard deviation of the effective radius were defined. The mean was the value of the effective radius at that layer for the current iteration. The standard deviation was 2 μm for the two uppermost and lowermost layers at cloud top and base. Every other layer in between was defined with a standard deviation of 1 μm. These values were based on results from the a priori dataset, which showed a greater variability in droplet size at cloud top and base than in the middle of the cloud.

To define the uncertainty of the assumed effective variance of the droplet size distribution, each in situ measured droplet profile was normalized along the vertical dimension and divided into 20 layers. With the ensemble of all measurements for each layer, a distribution shape and effective variance were solved for. We found that the effective variance decreases from cloud base to top, demonstrating that the droplet size distribution narrows with respect to altitude, a similar finding to previous studies [5]. We found the mean value of the effective variance at cloud top to be about 0.045, whereas the mean value at cloud base was about 0.1. libRadtran uses a precomputed table to convert cloud properties of droplet size and liquid water content to Mie properties to solve the radiative transfer equation, and this table is constructed assuming a single effective variance [38]. Therefore, the mean

value of all vertical profiles of effective variance, which was 0.055, was assumed in all our radiative transfer calculations. To account for the uncertainty caused by this assumption, the standard deviation of effective variance at each cloud level was determined from the a priori dataset. The values ranged from 0.05 at cloud bottom to 0.035 at cloud top.

To transform the forward model covariance matrix, S_{fm}, into measurement space, such that the measurement and forward model covariance matrices can be summed, $S_\epsilon = S_m + S_{fm}^{'}$, a forward model Jacobian is required:

$$S_{fm}^{'} = K_{fm} S_{fm} K_{fm}^{T} \tag{6}$$

Lastly, the contribution from each forward model uncertainty component on the total retrieval uncertainty can be quantified using

$$S_f = G_m K_{fm} S_{fm} K_{fm}^{T} G_m^{T} \tag{7}$$

where $G_m = {}^{\partial x}/_{\partial m}$ is the sensitivity of the retrieval to the measurement and is often called the Gain matrix [35].

2.7. Applying Retrieval to Real EMIT Measurements

The retrieval method described in Sections 2.1–2.6 was carefully developed for application to real measurements. After applying our GNOE retrieval to quasi-realistic simulated HySICS reflectance, we applied the retrieval to data from the EMIT hyperspectral imager flying on the ISS [34]. The only aspects of the retrieval method outlined in Sections 2.1–2.6 that were altered for application to EMIT measurements were the measurement covariance matrix and a few forward model assumptions. Only EMIT observations with spatiotemporally coincident observations from instruments onboard the Aqua satellite that were recorded within 10 min of one another were used in order to have a means of comparison.

We selected EMIT observations of clouds over the southeast Pacific off the coast of Chile, the same region surveyed during the VOCALS-REx field campaign, in order to confidently use the same a priori covariance matrix developed in Section 2.5. Applying the GNOE retrieval to different stratocumulus regions could lead to biases due to inherent differences in stratocumulus cloud regimes [53]. We adapted the Langley Automated Sensor Inter-calibration System (LASICS) tool [54] to find EMIT observations that overlap with MODIS, the Advanced Microwave Scanning Radiometer for EOS (AMSR-E) and Advanced Microwave Scanning Radiometer 2 (AMSR2) unified data products (AMSR-E/AMSR2 Unified), and the Atmospheric Infrared Sounder (AIRS). We searched the EMIT data record from its start on 1 January 2023 to 25 December 2025. We note that the comparison between remote retrievals derived from these instruments is not straightforward because each has a different sampling volume. Table 1 summarizes the spatial resolution of the EMIT spectral measurements and retrieved products from MODIS, AMSR-E/AMRS2 and AIRS.

Table 1. Each instrument used for the analysis in Section 3, along with a description of what each instrument was used for and the corresponding spatial resolution.

Instrument	Usage	Spatial Resolution at Nadir
EMIT	GNOE Hyperspectral retrieval	60 m (measurement resolution)
MODIS	Comparison of τ_c, LWP, and IWV_{ac}	~1 km (retrieval resolution)
AMSR-E/AMSR2	Comparison of LWP	~10 km (retrieval resolution)
AIRS	Comparison of IWV_{ac}	~50 km (retrieval resolution)

MODIS measurements of spectral reflectance in the visible and shortwave infrared are used to retrieve cloud effective radius, cloud optical thickness, and above-cloud integrated

water vapor [52,55] at a spatial resolution of approximately 1 km at nadir [52]. With a spatial resolution of 60 m, EMIT is capable of detecting spatial heterogeneity within a MODIS pixel. Therefore, the comparison between the retrieved variables from a single EMIT pixel and the retrieved variables from the overlapping MODIS pixel can be misleading. To address this, we randomly selected 30 EMIT pixels within each overlapping MODIS pixel to which our GNOE retrieval was applied. Comparing the retrieved variables over 30 pixels averages out any spatial heterogeneity within the overlapping MODIS pixel.

Microwave emission measurements are used to estimate cloud liquid water path [56,57], where ***LWP*** is proportional to the absorption of microwave emission along the path travelled. These retrievals are less sensitive to assumptions about droplet size distribution and droplet vertical structure than retrievals using visible and short wave infrared radiation [58]. This is one reason why retrievals of liquid water path derived from microwave emission measurements are often compared to estimates of ***LWP*** from Earth System Models [58,59]. The spatial resolution of the AMSR-E/AMSR2 Unified L2B Global Swath Ocean Product is approximately 10 km along track × 5 km across track, resulting in a much larger sampling volume than that of EMIT [57]. Given that microwave-derived estimates of ***LWP*** are more often compared with ***LWP*** estimates from Earth System Models, we wanted to compared the GNOE retrieval of liquid water path with the AMSR-E/AMSR2 Unified retrieval. However, we often found that the closest AMSR-E/AMSR2 Unified pixel was flagged as "Land/Bad Pixel". A previous study by Duncan et al. [60] found that land intrusions of 1–2% impact the retrieval, and that even side-lobe emission outside the nominal pixel field of view can be significant for observations near the coast. All of the EMIT observations used in this analysis were located near the coast because the EMIT instrument was designed to focus on dry-arid regions over land (most EMIT observations with high cloud fraction are thrown out). The number of available comparisons was so low as to be statistically meaningless. However, we used the few examples we had as a guide while developing the retrieval. Future work will use a larger dataset with more direct comparisons to microwave retrievals.

The AIRS instrument samples upwelling infrared radiation between 3.8 μm and 15 μm within 2378 spectral channels [61]. These measurements are used to retrieve vertical profiles of temperature and water vapor concentration, which are part of the AIRS version 7 Level 2 data products and have a spatial resolution of 50 km at nadir [62]. We used AIRS retrievals to define the vertical profile of temperature and water vapor concentration within the forward model of our retrieval. We also used the AIRS water vapor concentration retrieval as another means of comparison with the hyperspectral retrieval of above-cloud integrated water vapor.

Using MODIS retrievals, we filtered for observations of liquid water clouds with a cloud optical thickness greater than three and a maximum horizontal heterogeneity index of 2.5. Zhang and Platnick [63] showed the heterogeneity index, the ratio of the standard deviation of the 16 sub-pixels of MODIS-measured reflectance at 250 m spatial resolution to the mean, was a strong indicator of whether horizontal heterogeneity affected the retrieval of effective radius. The authors concluded that effective radius retrievals were biased when the cloud had a heterogeneity index greater than 0.3 [63]. Heterogeneity indices less than 0.1 are indicative of homogeneous scattering layers with negligible 3-D radiative biases [63]. We chose a heterogeneity threshold of 2.5 because we found very few coincident observations between EMIT and MODIS that met the smaller thresholds defined by [63]. This likely introduced 3-D biases in the retrieval. Future work will explore mitigation strategies for these biases.

Comparing retrievals from instruments with different spatial resolutions and different retrieval methodologies is an essential but fraught step in developing a new retrieval. The

usual approach is to compare against an established, well-characterized retrieval such as MODIS, but three differences must be kept in mind. First, all coincident observations used herein occur within 10 min of one another, so cloud microphysics may evolve between them. Second, each measurement samples over a unique and very different volume, so it represents average quantities, which for clouds may contain considerable spatial variability [64]. One previous study found the horizontal variability of effective radius in marine stratocumulus sampled during the VOCALS-REx in situ field campaign to be 0.31, 0.37, and 0.47 μm, for length scales of 0.5, 1, and 5 km respectively [20]. Third, the underlying radiative transfer models utilize different assumptions: for example, the MODIS bispectral retrieval assumes vertical homogeneity and results in a column-weighted effective radius representative of cloud top [19]; the method developed in this study assumes adiabatic droplet growth to retrieve effective radius at cloud top and base. The comparisons in Section 3.2 are, therefore, not validations. They remain useful because the legacy retrievals have been characterized for decades and their biases are documented.

2.8. Covariance Matrices and Forward Model Assumptions Used in EMIT Retrieval

We used 225 of the 285 EMIT spectral channels for the retrieval. On-orbit EMIT measurements have been compared to spectral measurements from two RadCalNet calibration and validation reference sites, revealing a discrepancy at wavelengths less than 500 nm, potentially due to calibration error [25]. An additional discrepancy was found near 1290 nm at the seam of two order sorting filters [25]. For these reasons, EMIT measurements less than 500 nm and between 1245 and 1320 nm were omitted in the analysis. Additionally, we omitted measurements with center wavelengths between 1357 nm and 1402 nm, and between 1826 nm and 1908 nm to avoid saturated water vapor absorption bands where the reflectance is near zero.

The EMIT spectral measurements were assumed to be independent from one another, resulting in a diagonal measurement covariance matrix where each element along the main diagonal was defined as the square of the reflectance uncertainty for that channel. The EMIT measurement uncertainty was determined by adding the EMIT measurement noise model [65] with an estimate for the absolute calibration error in quadrature. From two previous studies that investigated the on-orbit calibration of EMIT, we assumed a spectrally independent calibration uncertainty of 1.5% for all channels [25,66]. We note that a diagonal covariance matrix does not reflect the true nature of partial correlation between radiances across the spectrum, but it is a common simplifying assumption [22,23,36]. We used the same a priori matrix for the retrieved variables described in Section 2.5.

For each coincident observation, we used the MODIS-retrieved cloud top height [52] to constrain our forward model. The forward model covariance matrix accounts for the uncertainty in this quantity by using the in situ-derived statistics reported in Section 2.6. The forward model assumptions of effective variance described in Section 2.6 were used in the application with EMIT data, as was the forward model uncertainty accounting for a deviation in the assumed monotonic, adiabatic droplet profile.

3. Results

3.1. Retrievals Using Simulated HySICS Reflectance

First, we applied our retrieval to simulated HySICS reflectance from clouds with smooth, monotonic droplet profiles, removing forward model uncertainty caused by deviations from these ideal profiles (see Section 2.2). With negligible forward model uncertainty, we retrieved r_{top}, r_{bot} and τ_c, and made an assumption about the water vapor profile, a common assumption in most retrievals of cloud droplet size [18,22,36,44]. These results highlight the impact of assuming a water vapor profile, and, therefore, the IWV_{ac}, on

the retrieval of droplet size at cloud top and base. Next, we applied our retrieval to the simulated reflectance dataset constructed from the VOCALS-REx in situ measurements. These measurements simulate more realistic clouds and the forward model uncertainties that are encountered when using real data. We quantify the performance of the retrieval by computing the average percent difference in LWP between our GNOE retrieval and the TBLUT estimate, the modified TBLUT estimate by Wood and Hartmann [67], and the in situ value.

A proper comparison between the hyperspectral GNOE retrieval and the in situ measurements should include uncertainty in measured droplet size. However, the CDP droplet size uncertainty estimate is attributed to several factors that make it difficult to quantify [51]. Lance et al. [51] used a water droplet generating system to determine the sizing accuracy of the CDP instrument. Using their results, we simplified the CDP measurement uncertainty for this analysis by defining an uncertainty of 20% for effective radii below 5 μm, 15% for radii greater than 5 μm and less than 10 μm, and 10% for radii greater than or equal to 10 μm.

3.1.1. Incorrect Assumptions of Water Vapor Profile Impact the Droplet Profile Retrieval

If above-cloud integrated water vapor is not retrieved, an assumption must be made. Figure 3 shows the impact of different forward model errors of above-cloud integrated water vapor on the droplet profile retrieval. The retrieval algorithm of Buggee and Pilewskie [20], which used 35 wavelengths outside of water vapor absorption regions, was applied to about 800 synthetic HySICS reflectance spectra where forward model uncertainty was negligible, except for the above-cloud integrated water vapor. Between spectra, cloud optical thickness, cloud droplet profile and solar/viewing geometry varied. Retrievals were performed with four different assumptions of IWV_{ac}. The retrieval bias for the effective radius at cloud top, shown in panel (a), is at most 0.4 μm, less than the average MODIS retrieval uncertainty for marine stratocumulus analyzed in this study of about 0.9 μm. Despite the small magnitude, Figure 3a reveals a consistent pattern. When the assumed integrated water vapor content exceeds/is less than the true value, the retrieval compensates for the excess/insufficient absorption due to water vapor by reducing/increasing retrieved droplet sizes at cloud top. We note that the retrieval bias is not zero when the true and assumed IWV_{ac} are equal because the synthetic reflectance used in the retrievals was computed with 0.3% Gaussian uncertainty. The combination of retrieval uncertainty due to the initial guess and the measurement uncertainty leads to an imperfect retrieval. Panel (b) shows a much larger spread in retrieval bias for the effective radius at cloud bottom, with a maximum value approaching 1 μm.

The different error trends arise from where in the cloud the two effective radii are constrained by the measurements. As the weighting functions in Figure 1 show, the reflected signal, particularly near water vapor absorption features, is weighted toward cloud top, so the effective radius at cloud top is well constrained, and its bias responds nearly linearly to an error in the assumed above-cloud water vapor. The effective radius at cloud base is constrained by the comparatively few photons that penetrate deeper into the cloud, where the signal is weaker. The retrieval bias due to uncertainty in the assumed above-cloud integrated water vapor is therefore larger in magnitude, and saturates once the above-cloud water vapor becomes larger than about 8 mm. In addition, bias in the retrieved effective radius at cloud base is even more susceptible to the measurement uncertainty; we reduced all sources of forward model uncertainty, but measurement uncertainty will still lead to an imperfect retrieval, and this impact is greater for droplet sizes retrieved at cloud base than at cloud top.

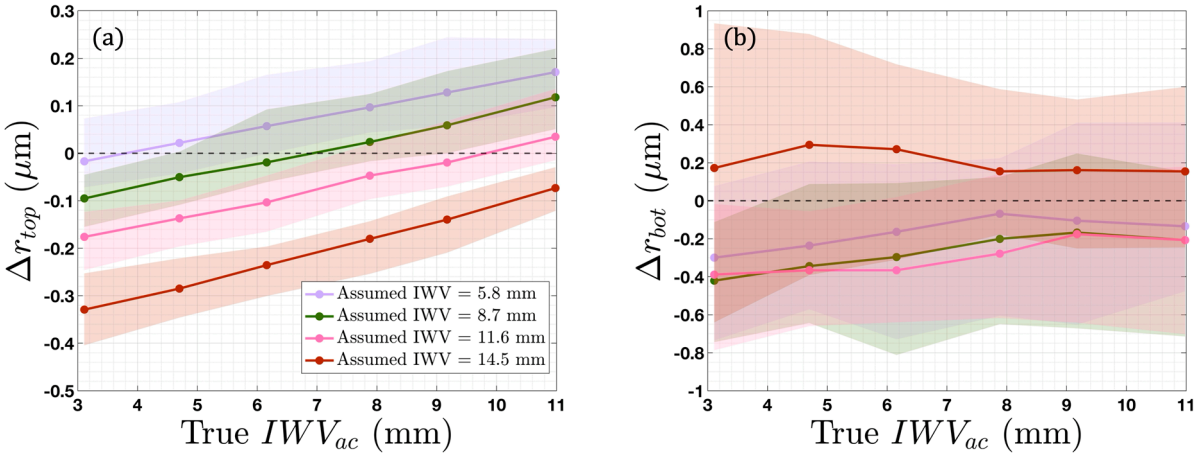


Figure 3. Retrieval bias, defined as the difference between the retrieved variable and the true value, for the effective radii at cloud top (**a**) and base (**b**). The true integrated water vapor content above cloud is the amount used to compute simulated HySICS reflectance. The four colored lines represent the four different assumptions of integrated water vapor content for the retrieval. The solid line represents the median and the shaded area represents the 25th and 75th percentile for about 800 retrievals (see Section 3.1). The dashed line represents a retrieval bias of 0 µm.

3.1.2. Assessment of Retrieval Performance

The retrieval method was then applied to the set of simulated HySICS reflectance with cloud microphysics defined using VOCALS-REx in situ measurements (see Section 2.2). Figure 4 shows three examples of retrieved profiles from the 69 simulated reflectance spectra, chosen to highlight distinct cases: (a) rapid change at cloud base, (b) minimal fluctuations throughout, and (c) rapid change at cloud top. While the retrieved droplet profiles are not capable of representing these rapid fluctuations in droplet effective radius, the retrieved profiles closely follow the in situ measurements. The three cases shown in Figure 4 demonstrate close agreement between the in situ measured above-cloud integrated water vapor content and the retrieved value.

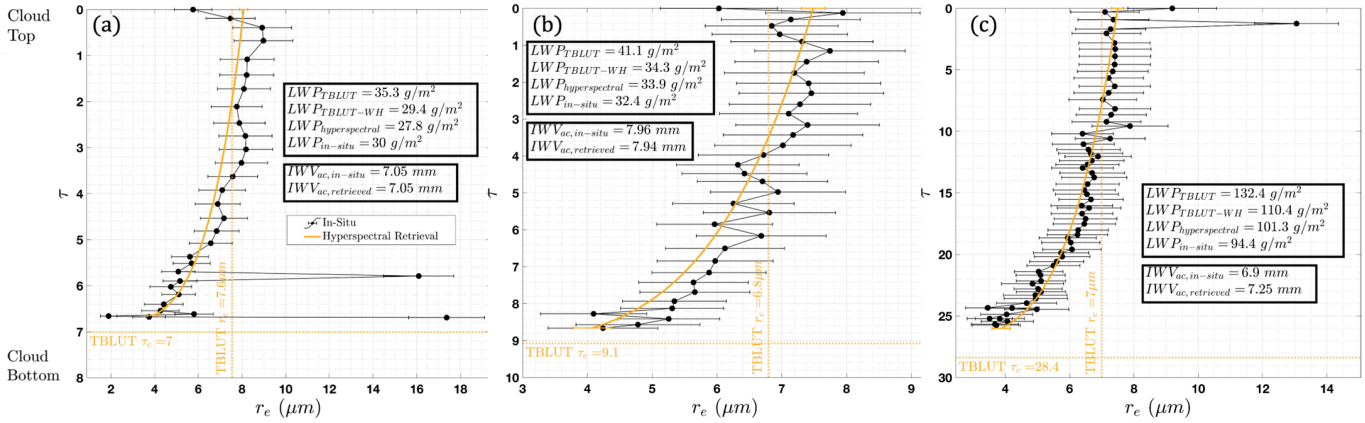


Figure 4. Panels (**a**–**c**) show three different comparisons of in situ measurements that were used to simulate HySICS reflectance, and the associated TBLUT and GNOE retrievals. The in situ measured effective radius (black circles), TBLUT effective radius retrieval (dotted yellow lines), and the GNOE retrieved vertical profile (solid yellow curve) are shown in each panel. Text boxes compare liquid water path estimates between in situ measurements and three retrieval methods: TBLUT (Equation (8)), TBLUT with Wood–Hartmann adjustment (Equation (9)), and our GNOE hyperspectral retrieval (Equation (10)). Also shown is the in situ and retrieved above-cloud integrated water vapor. Yellow horizontal bars indicate retrieval uncertainty for effective radius at cloud top and base. Black horizontal bars indicate the in situ measurement uncertainty.

The largest discrepancy in IWV_{ac} shown is for the example with an optical thickness of 28.2, in panel (c). We know from Albert et al. [47] that the retrieval of IWV_{ac} will likely overestimate the true value for optically thick clouds due to the apparent elongation of the water vapor path due to multiple scattering.

Table 2 reports the comparison of each retrieved variable against the in situ measured value across all 69 simulated cases, showing the average percent difference (%) and the average difference (μm or mm). In situ r_{top} and r_{bot} were defined as the average effective radius over the top and bottom 25% of each in situ measured vertical profile with respect to the normalized altitude within cloud in order to average over rapid vertical fluctuations in $r_e(z)$. The retrieval of effective radius at cloud top was found to be the closest to in situ measurements, with an average percent difference of −0.4% (−0.01 μm). The retrieval of effective radius at cloud bottom has the largest average percent difference against the in situ measurements, with a value of 21.4% (1.4 μm). The retrievals of above-cloud integrated water vapor and cloud optical thickness were found to be similar to the in situ measured values, with average percent differences of −1.2% (−0.09 mm) and −0.015% (−0.012) respectively. The retrieval error at cloud base was expected to be larger than at cloud top, since we know from analysis with weighting functions that there is little signal from cloud base. In addition, cloud base is where droplet growth is most prominent, and there are often fluctuations in droplet size (see Figure 4a), both of which contribute to the in situ measured r_{bot} being larger than the retrieved value by about 1.4 μm, on average. Nevertheless, the results in this table provided confidence that the GNOE retrieval is accurate when applied to synthetic HySICS reflectance where the measurement and forward model uncertainty was precisely known.

Table 2. Average percent difference (%) and average difference (μm for r_{top} and r_{bot} and mm for IWV_{ac}) between the in situ measured values and the retrieved quantities of droplet effective radius at cloud top and base, above-cloud integrated water vapor, and cloud optical thickness. $N = 69$ comparisons.

In Situ Measurement—GNOE Retrieval	Avg. % Difference (%)	Avg. Difference (Absolute Units)
Droplet Size at Cloud Bottom (r_{top})	−0.4%	−0.01 μm
Droplet Size at Cloud Bottom (r_{bot})	21.4%	1.4 μm
Above-cloud Integrated Water Vapor (IWV_{ac})	−1.2%	−0.09 mm
Cloud Optical Thickness (τ_c)	−0.015%	−0.012

Cloud optical thickness was found to be correlated with the difference between the in situ measured effective radius at cloud bottom and the retrieved value, with a Pearson correlation value (which measures the strength of a linear association) of $r = -0.17$ and a Spearman correlation (which measures monotonic association independent of linearity) value of $\rho = -0.318$. A larger Spearman than Pearson correlation value implies there is a monotonic relationship that is likely non-linear. This finding is reinforced by those of King and Vaughn [23], who showed a direct relationship with retrieval uncertainty of droplet size at cloud base with cloud optical thickness. Larger optical thicknesses reduce retrieval sensitivity to droplet size at cloud base, as shown by Buggee and Pilewskie [20]. The Pearson correlation between the cloud optical thickness and the retrieval error of droplet size at cloud top was $r = 0.187$ with a Spearman correlation of $\rho = 0.003$. This is indicative of a non-linear relationship with an interior minimum, similar to the results of King and Vaughan [23].

The average percent difference between the liquid water path derived from in situ measurements and values derived from three different retrievals is listed in Table 3. Assuming vertically constant droplet number concentration and that the size parameter, $x = 2\pi r/\lambda$, is much larger than unity, liquid water path can be estimated as the product of effective radius and cloud optical thickness:

$$LWP = \frac{2}{3}\rho\ \tau_c\ r_e \tag{8}$$

where ρ is liquid water density. This expression forms the basis for liquid water path estimates in the MODIS Collection 6 cloud products [68], referred to hereafter as TBLUT LWP. Several studies have shown that retrieving liquid water path from visible/shortwave infrared retrievals of cloud optical properties using Equation (8) results in an overestimation compared to retrievals of liquid water path using measurements of microwave emission [11,58,69].

Table 3. Average percent difference (%) and average difference (g/m^2) between the in situ measured values of liquid water path ($N = 69$) and three different retrievals.

Liquid Water Path Retrieval	Avg. % Difference (%)	Avg. Difference (g/m^2)
In situ measurement—HySICS GNOE retrieval	−26.9%	−11.6 g/m^2
In situ measurement—TBLUT retrieval	−45.2%	−20.3 g/m^2
In situ measurement—TBLUT retrieval w/Wood–Hartmann adjustment	−21.1%	−8.4 g/m^2

An adjustment to the TBLUT LWP estimate by assuming vertical variation in droplet size results in values closer to microwave retrievals [11]. Wood and Hartmann [67] derived a modified expression for adiabatic clouds, where liquid water content varies linearly with height:

$$LWP = \frac{5}{9}\rho\ \tau_c\ r_e \tag{9}$$

Equation (9) will be referred to as the TBLUT LWP_{WH} estimate for the remainder of the paper. To estimate liquid water path from retrieved droplet profiles, we assumed that droplet number concentration was constant with altitude, an assumption in line with analysis of in situ measurements by Buggee and Pilewskie [20]. This enables us to solve for liquid water path without needing to know the droplet number concentration by substituting it with the equation for cloud optical thickness. Assuming the size parameter, $x = 2\ \pi\ r/\lambda$, is much greater than 1, we use the geometric optics approximation, defining the extinction efficiency parameter as $Q_{ext} = 2$, resulting in the following simplified expression (see [70] for full derivation):

$$LWP = \frac{2}{3}\rho\ \tau_c \frac{\int r_e(z)^3\ dz}{\int r_e(z)^2\ dz} \tag{10}$$

The true in situ measured LWP used to compute the synthetic HySICS reflectance was compared to the GNOE retrieved LWP, the TBLUT LWP (Equation (8)), and Wood–Hartmann adjusted TBLUT LWP (Equation (9)). The results in Table 3 demonstrate that the GNOE retrieval applied to the full synthetic HySICS reflectance spectrum achieved better agreement with in situ measurements, with a −26.9% average difference (−11.6 g/m^2) compared to the standard TBLUT method of −45.2% (−20.3 g/m^2). The Wood–Hartmann adjustment substantially improves the TBLUT estimate, with an average percent difference of −21.1% (−8.4 g/m^2), exceeding the performance of the values derived from our

retrieved droplet profile. This suggests that accounting for vertical droplet size variation, whether through the simplified Wood–Hartmann correction or retrieving the full profile retrieval, is essential for accurate LWP estimation. We note that all three retrieved products overestimate the in situ measured LWP, on average.

Figure 5 shows comparisons between the GNOE retrievals of LWP, the TBLUT LWP retrievals, τ_c, and IWV_{ac} with the true in situ measured values used to create the measurements. Panel (a) reinforces Table 3, showing that the GNOE retrieval of LWP exhibits a small, positive bias. This bias likely reflects two limitations of the retrieval. First, we assumed adiabatic droplet growth within the cloud, a good approximation but not a perfect representation of the in situ measurements used to create the synthetic reflectance. Second, rapid vertical fluctuations in droplet size are not captured. Together, these lead to discrepancies in the retrieved and in situ LWP. Panel (b) shows the TBLUT LWP estimate exhibits a positive bias, with the slope of the linear fit about 11% larger than the value for the hyperspectral retrieval. Previous studies have found similar biases between TBLUT retrievals of LWP and in situ measurements due to the assumption of vertical homogeneity [11]. Panel (c) shows that the Wood–Hartmann adjustment leads to a more accurate LWP estimate, with the slope of the linear fit about 7% smaller than that for our GNOE retrieval. These results are similar to those of Seethala and Horváth [11], who showed better agreement between MODIS-derived retrievals of LWP and retrievals from microwave emission measurements using the Wood–Hartmann adjustment. Panel (d) shows that the hyperspectral retrieval of cloud optical thickness is accurate across the range shown here, with a small bias of 0.2%. While the mean percent difference in Table 2 is −1.2% (−0.09 mm), Figure 5e shows the linear fit between the retrieval and the true value has a non-zero offset, predominantly related to τ_c. When comparing the percent difference between the retrieved and in situ IWV_{ac} with cloud optical thickness, we found a Pearson correlation of $r = 0.872$ and a Spearman correlation of $\rho = 0.868$. Since $r \approx \rho$, the relationship is linear. The signed (as opposed to absolute) percent difference is negative below $\tau_c \approx 9$, and positive above. These results are in agreement with Albert et al. [47], who determined that IWV_{ac} tends to be overestimated for optically thick clouds.

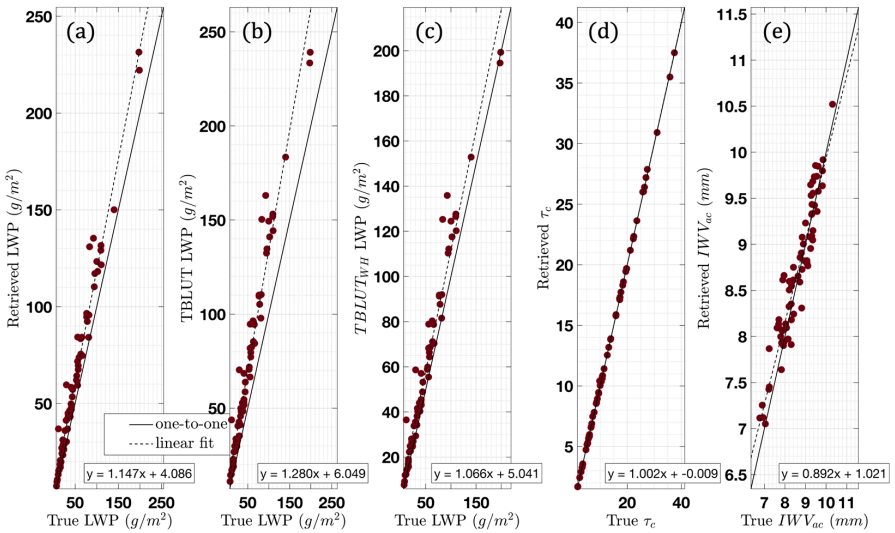


Figure 5. Performance of the (**a**) GNOE hyperspectral LWP retrieval, (**b**) the TBLUT LWP, (**c**) the TBLUT LWP retrieval with the Wood–Hartmann adjustment, and the GNOE retrieval of (**d**) cloud optical thickness, and (**e**) above-cloud integrated water vapor. These retrievals used simulated HySICS reflectance. The true in situ measured value is shown on the x-axis. The solid line represents perfect agreement; a one-to-one line. The dashed line is the linear fit, mathematically described in the lower right-hand box.

3.2. Retrievals Using EMIT Measurements

Figure 6 shows an example scene from one of the 3695 EMIT measurements used for this analysis. While we always found many EMIT pixels completely contained within a MODIS pixel, the MODIS pixels often straddled, or at times were outside of, the closest AMSR-E/AMSR2 Unified retrieval footprint. The AIRS Level 2 retrieval footprint is so much larger than the other instrument footprints that it often included non-cloudy regions or regions over land (see Table 1). This figure highlights the different ground sampled areas between EMIT, MODIS, AMSR-E/AMSR2 and AIRS, demonstrating the difficulty with comparing retrievals from each. We again note that comparisons in this section are not validations, but remain useful because the legacy retrievals have been characterized for decades and their biases are documented.

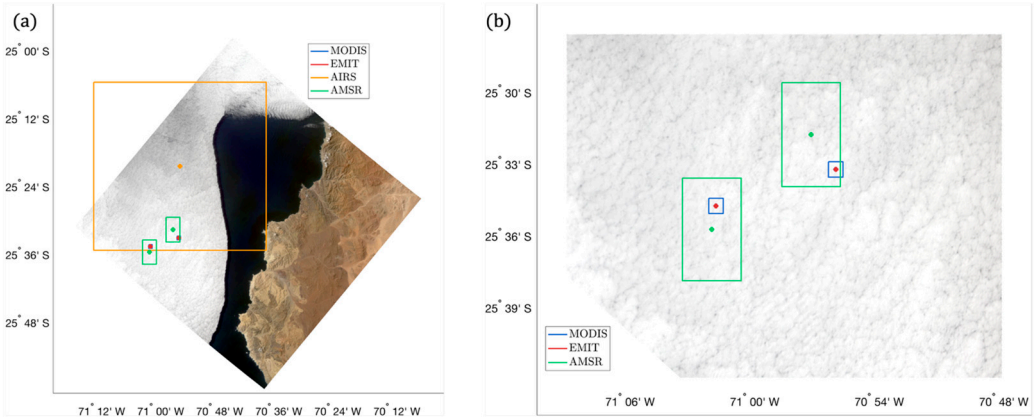


Figure 6. Panel (**a**) shows an EMIT swath recorded on 16 September 2023 at 19:11:30 UTC, off the coast of Chile. The orange box shows an approximation of the closest AIRS Level 2 standard retrieval footprint in space and time to the EMIT measurements, shown in red. The green boxes show an approximation for the closest AMSR-E/AMSR2 Unified Level 2 Global Swath Ocean Product footprint to each EMIT measurement shown in red. Panel (**b**) is a cropped version of panel (**a**) to highlight the closest MODIS Level 2 retrieval, with the footprint approximated by the blue boxes.

Three examples of retrieved droplet profiles using EMIT measurements are shown in Figure 7. Without coincident in situ measurements, we compared these retrievals with the liquid water path retrieved from MODIS and AMSR-E/AMSR2 Unified measurements (when available), and the above cloud integrated water vapor retrieved from MODIS and AIRS measurements. Panel (a) is the only example shown with a usable overlapping AMSR-E/AMSR2 Unified retrieval of liquid water path. The average percent difference between the MODIS retrieved effective radius and the hyperspectral retrieval of effective radius at cloud top was 10.3% (1.2 μm), implying that the value derived from MODIS measurements typically exceeded the hyperspectral retrieval of effective radius at cloud top. We expected these values to be similar because of the MODIS retrieval bias towards droplet sizes at cloud top, as depicted in Figure 7. While the three examples shown in Figure 7 show close agreement between the hyperspectral retrieval of optical thickness and the MODIS retrieved value, we found the hyperspectral retrieval of optical thickness to vary spatially within all of the MODIS scenes used for this analysis, which is why we ran our retrieval on 30 different EMIT pixel measurements within each MODIS pixel used in this analysis. This was done in order to average out this spatial heterogeneity.

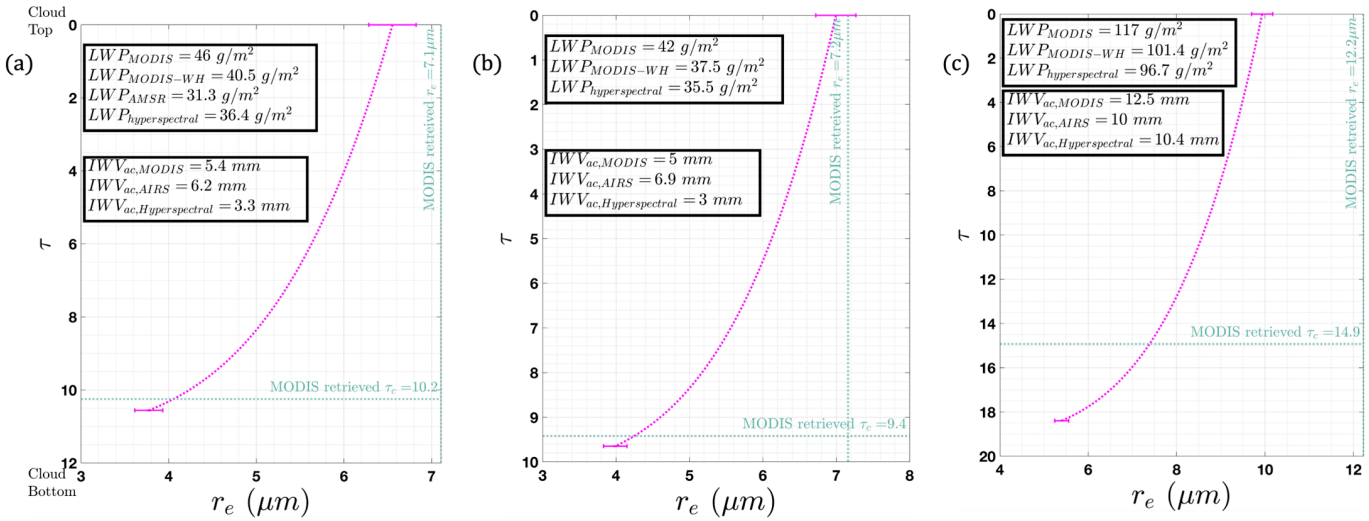


Figure 7. Panels (**a**–**c**) show three different comparisons of coincident retrievals between MODIS and our GNOE retrieval applied to EMIT measurements. The MODIS retrieval (dotted green lines) and the retrieved vertical profile using EMIT spectral channels (pink curve). Pink horizontal bars indicate retrieval uncertainty for effective radius at cloud top and bottom. Upper boxes compare the hyperspectral retrieval of LWP (Equation (10)) with the MODIS retrieval (Equation (8)), the MODIS retrieval with the Wood–Hartmann adjustment (Equation (9)), and the AMSR-E/2 microwave retrieval (if available). Lower boxes compare the hyperspectral retrieval of above-cloud integrated water vapor with the MODIS and AIRS estimates.

The average percent difference between the MODIS retrieval of liquid water path and the MODIS retrieval with the Wood–Hartmann adjustment with our GNOE retrieval using EMIT measurements is reported in Table 4. These results show that the MODIS retrieval, which assumes a vertically homogeneous cloud, estimates cloud liquid water 19% larger, on average, than our estimate derived from the retrieved vertical droplet profile. While we were not able to compare our retrieval of liquid water path with retrievals from AMSR-E/AMSR2 often enough to report meaningful statistics, we note that previous work has reported a positive bias between MODIS and AMSR-E for overcast scenes, implying that our GNOE hyperspectral retrieval of liquid water path reported in Table 4 should be closer to retrievals derived from microwave measurements than the TBLUT estimates [11]. The MODIS retrieval of liquid water path with the Wood–Hartmann adjustment was found to be 2.9% larger than our estimate, on average. This reinforces previous work that demonstrated this adjustment led to liquid water path retrievals in better agreement with retrievals derived from microwave measurements, which are thought to be a better representation of liquid water path [11].

Table 4. The average percent difference (%) and average difference (g/m^2) between the MODIS-derived liquid water path (Equation (8)) and the GNOE retrieval using EMIT measurements. A similar comparison with the MODIS-derived liquid water path using the Wood–Hartmann adjustment is also shown (Equation (9)). $N = 3695$ comparisons.

Liquid Water Path Retrieval Comparison	Avg. % Difference (%)	Avg. Difference (g/m^2)
MODIS retrieval—EMIT GNOE retrieval	19%	15.6 g/m^2
MODIS retrieval w/Wood–Hartmann adjustment—EMIT GNOE retrieval	2.9%	2.2 g/m^2

Table 5 summarizes the comparison between the MODIS and AIRS retrievals for above-cloud integrated water vapor content and the MODIS retrieval of cloud optical

thickness with our GNOE retrieval applied to EMIT measurements. We found that the retrievals of IWV_{ac} from MODIS and AIRS measurements were, on average, greater than our GNOE retrieval by 24.3% and 21.4%, respectively. This bias may be due to inherent differences between the three retrievals. The comparison with the MODIS-derived near-infrared column water vapor retrieval is best understood as a comparison between two independent retrievals rather than a bias assessment against a reference truth. Over the optically thick marine stratocumulus considered in this paper, the MODIS near-IR product does not report a geophysical above-cloud column water vapor amount. For low water clouds, the algorithm retrieves an "effective" precipitable water assuming the cloud top lies at sea level [55]. In addition, the product carries no per-pixel uncertainty. The positive bias of 24.3% is likely due to retrieval methodology differences. The water vapor product derived from AIRS measurements retrieves a cloud-cleared, full-column moisture profile at ~45 km spatial resolution with coarse information content in the lower troposphere (a few broad layers) [71]. The enormous difference in sampling volume also likely contributes to the retrieval differences between AIRS and our GNOE retrieval. The MODIS retrieval of IWV_{ac} was found to be 7.7% smaller, on average, than the retrieval derived from AIRS measurements. Table 5 also demonstrates a strong similarity between the MODIS retrieval of cloud optical thickness and our value derived from the GNOE retrieval. The MODIS-derived values were found to be 6.6% smaller than our estimates, on average.

Table 5. The average percent difference (%) and average difference (mm) between the MODIS- and AIRS-derived above-cloud integrated water vapor content and the GNOE retrieval. A similar comparison between the MODIS-derived cloud optical thickness and the GNOE retrieval is shown in the last row. $N = 3695$ comparisons.

Above-cloud Integrated Water Vapor	**Avg. % Difference (%)**	**Avg. Difference (mm)**
MODIS retrieval—EMIT GNOE retrieval	24.3%	1.9 mm
AIRS retrieval—EMIT GNOE retrieval	21.4%	1.8 mm
MODIS retrieval—AIRS retrieval	−7.2%	0.1 mm
Cloud Optical Thickness	**Avg. % Difference (%)**	**Avg. Difference**
MODIS retrieval—EMIT GNOE retrieval	−6.6%	−0.82

The impact of forward-model uncertainty on the total retrieval uncertainty was quantified using Equation (7) and summarized in Table 6. Forward-model assumptions contribute unequally to the four retrieved quantities. The assumed uncertainties in the three forward-model parameters, an adiabatic r_e profile, cloud top height, and droplet effective variance, are mapped into the retrieval-error covariance through the gain matrix following Rodgers [35]. Median values across the 3695 retrieved pixels show that forward-model assumptions account for 58% of the total retrieval-error variance in r_{top}, but only 14% in τ_c, 7.7% in r_{bot}, and 3.7% in IWV_{ac}. The dominant sources of forward model uncertainty for the radius at cloud top were the adiabatic-profile assumption (34% of the total variance) and the droplet effective variance (24%). For the remaining variables, a single source dominates the comparatively smaller contribution of forward model uncertainty to the total variance. The radius at cloud bottom was found to be dominated by the a priori and its uncertainty, rather the forward model uncertainty.

Table 6. Impact of forward model uncertainty on the retrieval uncertainty of the four retrieved variables.

Variable	Forward Model Share of Total Variance	Dominant Source(s) (% of Total Variance)
r_{top}	58%	adiabatic profile (34%) + effective variance (24%)
r_{bot}	7.7%	adiabatic profile (4.1%)
τ_c	14%	adiabatic profile (13.8%)
IWV_{ac}	3.7%	cloud top height (2.6%)

4. Summary and Discussion

We developed an optimal estimation retrieval method to simultaneously retrieve vertical profiles of cloud droplet effective radius, cloud optical thickness, and above-cloud integrated water vapor from hyperspectral measurements in the visible and shortwave infrared. Four aspects of this work have not previously been demonstrated in the context of a droplet-profile retrieval: (1) retrieving vertical droplet profiles from real (that is, rather than synthetic, as in previous studies) hyperspectral measurements and comparing them with values derived from MODIS and AIRS, (2) transformation of the Gauss–Newton problem into logarithmic space to better represent the log-normal distributions of retrieved variables, (3) computation of the a priori covariance matrix including off-diagonal elements using in situ measurements and ERA5 reanalysis data, and (4) incorporation of forward model uncertainty through a forward model Jacobian that accounts for deviations from assumed smooth adiabatic profiles, uncertainty in cloud top height, and uncertainty in the assumed effective variance of the droplet size distribution.

The physical basis for simultaneously retrieving above-cloud integrated water vapor stems from the work of Albert et al. [47], who showed that for optically thick marine clouds over the ocean, the dominant contribution to water vapor absorption comes from the atmospheric column above the cloud rather than below. We leveraged this by including spectral measurements in the wings of water vapor absorption features, which provide additional information content for constraining both the droplet profile [23,29]. Figure 1 demonstrated that weighting functions derived from HySICS spectral channels near water vapor absorption features exhibit greater relative orthogonality compared to channels outside these features, with wavelengths closer to strong absorption bands shifting the proportion of scattered photons toward cloud top. This enhanced orthogonality is fundamental to the ability to retrieve both the droplet profile and above-cloud integrated water vapor.

The impact of incorrectly assuming above-cloud integrated water vapor on droplet profile retrievals using simulated HySICS reflectance with smooth, monotonic adiabatic profiles was quantified in Figure 3. For the examples shown in Figure 3, retrieval bias for radii at cloud top and base reached values of approximately 0.4 μm and 1 μm, respectively. When the assumed $\boldsymbol{IWV_{ac}}$ exceeded the true value, the retrieval compensated for the excess absorption by converging toward smaller droplet sizes. Conversely, when the assumed $\boldsymbol{IWV_{ac}}$ was less than the true value, the algorithm converged toward larger droplet sizes. These results demonstrated that accurate droplet profile retrievals require simultaneous estimation of above-cloud integrated water vapor rather than relying on climatological assumptions.

We tested our retrieval method on 69 simulated HySICS reflectance spectra constructed using VOCALS-REx in situ measurements of cloud microphysics. This quasi-realistic dataset enabled systematic evaluation of retrieval performance against true values while maintaining precise control over forward model uncertainties. To quantify overall retrieval performance, the four retrieved variables were compared against the in situ values in Table 2. The retrieval errors for the effective radius at cloud top, the above-cloud integrated

water vapor, and cloud optical thickness were −0.4%, −1.2%, and −0.0015%, respectively. Effective radius at cloud base had the highest retrieval error of 21.4%, consistent with the low signal-to-noise from this region of the cloud (Figure 1). Three liquid water path estimates were also compared with in situ measurements: the estimate derived from our GNOE retrieval (Equation (10)), the standard TBLUT method (Equation (8)), and the Wood–Hartmann adjusted TBLUT method (Equation (9)). Table 3 demonstrates that the in situ measurement and our GNOE retrieval had an average percent difference of −26.9%, substantially better than the standard TBLUT method (45.2%). The Wood–Hartmann adjustment, which accounts for a linear increase in liquid water content with height, improved the TBLUT estimate to 21.1%, a similar value to the GNOE retrieval. This result is consistent with previous studies showing that accounting for vertical droplet size variation is essential for accurate $\boldsymbol{LWP}$ estimation [11,23]. Figure 5 revealed that while the GNOE $\boldsymbol{LWP}$ retrieval exhibited a small positive bias overall, retrieval accuracy diminished for large in situ $\boldsymbol{LWP}$ values exceeding approximately 100 g/m^2. This degradation likely reflects increased forward model uncertainty for optically thicker clouds, where photon penetration into the lower cloud layers becomes more limited and the uncertainty for the retrieved droplet radius at cloud base increases. Cloud optical thickness retrievals (Figure 5d) showed excellent agreement across all magnitudes, with retrieved values closely following the one-to-one line. Above-cloud integrated water vapor retrievals (Figure 5e) demonstrated accurate performance, though future work with a larger in situ dataset spanning a wider range of $\boldsymbol{IWV_{ac}}$ values will enable more robust assessment across diverse atmospheric conditions.

The transformation of the retrieval problem into logarithmic space proved essential for improving convergence. All four retrieved variables—effective radii at cloud top and base, cloud optical thickness, and above-cloud integrated water vapor—more closely followed log-normal distributions than normal distributions, with $\boldsymbol{R^2}$ values higher in log space. This finding is consistent with previous studies showing that many atmospheric variables are inherently non-negative and better represented by log-normal distributions [32,33]. The a priori covariance matrix computed from VOCALS-REx in situ measurements revealed physically meaningful correlations: effective radius at cloud top was found to have positive correlation coefficients with effective radius at cloud base (0.57) and cloud optical thickness (0.21). Interestingly, cloud optical thickness was found to have a higher correlation coefficient with the effective radius at cloud base (0.30) than at cloud top. Above-cloud integrated water vapor content was found to have weak correlation coefficients with effective radii at cloud top (−0.09), cloud base (−0.1) and cloud optical thickness (−0.12). The specific mechanisms driving these correlations warrant further investigation with larger in situ datasets.

Application of our retrieval method to hyperspectral measurements from the EMIT imaging spectrometer provided an initial demonstration of performance on real data, using coincident observations from MODIS and AIRS for comparison. EMIT, with a spectral range similar to HySICS but with coarser spectral resolution (285 vs. 636 channels) and larger radiometric uncertainty (~1.5% assumed vs. 0.3% for HySICS), served as a surrogate for the upcoming CLARREO Pathfinder instrument. Table 4 shows the results from applying our retrieval to 3695 EMIT pixels. We found that the MODIS retrieval, which assumes vertically homogeneous clouds, estimated $\boldsymbol{LWP}$ 19% larger, on average, than our estimate derived from the retrieved droplet profile. The MODIS $\boldsymbol{LWP}$ with the Wood–Hartmann adjustment was 2.9% larger than our hyperspectral estimate, consistent with the direction and approximate magnitude of biases observed in previous studies [11].

The retrieval of above-cloud integrated water vapor from EMIT measurements was consistently lower than estimates from both MODIS and AIRS by 24.3% and 21.4%, respec-

tively. This systematic underestimation is likely due to inherent differences between the three retrievals. Over optically thick marine stratocumulus, the MODIS near-IR water vapor product does not report a geophysical above-cloud column amount. For low water clouds, the algorithm retrieves an "effective" precipitable water assuming the cloud top lies at sea level [55]. In addition, the product carries no per-pixel uncertainty. AIRS does not measure above-cloud water vapor directly; it retrieves a cloud-cleared, full-column moisture profile at ~50 km spatial resolution between the surface and upper troposphere [71]. Therefore, the results from Table 5 are best thought of as comparisons, not validations. We also note that the MODIS retrieval of column-integrated water vapor was, on average, 7.7% smaller than the AIRS-derived retrieval, indicating differences between the instruments that highlight the complication of direct validation. Future work should carefully characterize the sources of these biases, including the contribution of the a priori and the spatiotemporal representativeness of the comparison datasets.

Taken together, the comparison between simulated HySICS reflectance and real EMIT observations highlights how instrument characteristics directly affect retrieval performance. The larger radiometric uncertainty and coarser spectral resolution contribute to the degraded retrieval performance of liquid water path and above-cloud integrated water vapor content relative to simulated results. Nevertheless, the liquid water path and effective radius retrievals from EMIT remain physically consistent with coincident MODIS observations and reproduce the expected direction of the TBLUT bias, providing confidence that the retrieval methodology transfers successfully from simulated to real hyperspectral data. The HySICS instrument, with its order-of-magnitude improvement in radiometric accuracy over EMIT and nearly twice the number of spectral channels, is expected to improve overall performance relative to the EMIT results presented here.

Several limitations of this study warrant discussion. There were no in situ droplet profile measurements over the southeast Pacific coincident with the EMIT observations used in this analysis, so the retrieved EMIT droplet profiles themselves are not compared against measured profiles. This is precisely why the method is first evaluated against simulated HySICS reflectance constructed from VOCALS-REx in situ microphysics (Section 3.1), where the true profile is known and the retrieval error can be quantified directly (Table 2). For the EMIT application, we restricted the analysis to observations spatiotemporally coincident with instruments aboard Aqua that met our criteria of non-precipitating liquid clouds with $\tau_c \geq 3$ and the heterogeneity index $H_\sigma \leq 2.5$. Selecting 30 EMIT pixels within each of the coincident MODIS pixels (of which there were about 125) that met the aforementioned criteria led to 3695 retrieval comparisons over the southeast Pacific between 1 January 2023 and 25 December 2025 (some retrievals failed, resulting in fewer than 30 retrievals for some of the coincident MODIS observations). This permitted comparison of liquid water path, which is derived from the retrieved droplet profile. Agreement in liquid water path provides an indirect constraint on the profile, though not a substitute for a direct comparison.

Our forward model assumes 1-D plane-parallel radiative transfer, which does not accurately represent all cloud regimes. Horizontally inhomogeneous clouds can lead to 3-D radiative effects such as illumination and shadowing from net horizontal radiative transport. Previous studies have shown that horizontal heterogeneity increases uncertainty in retrieved effective radius [63,72]. To limit these effects, EMIT observations with coincident MODIS-derived cloud heterogeneity indices of less than 2.5 were used, though this threshold is substantially higher than the value of 0.3 recommended by Zhang and Platnick [63] for avoiding 3-D biases. A higher threshold was used to increase the number of observations that could be used in this analysis. Future work should explore more sophisticated approaches for identifying and correcting 3-D radiative effects in hyperspectral retrievals.

We relied on a relatively small set of in situ observations ($N = 69$) from a single field campaign conducted over a limited spatial region. The VOCALS-REx campaign surveyed marine stratus and stratocumulus clouds off the coast of Chile in the southeast Pacific from October to November 2008, representing only one cloud regime under specific meteorological conditions. While this region is ideal for studying these cloud types due to their prevalence and relative homogeneity, the a priori covariance matrix derived from these measurements may not be representative of marine boundary layer clouds in other regions or under different synoptic conditions. For instance, clouds over the northeast Pacific, the Southern Ocean, or the Namibian coast may exhibit different relationships between droplet size, cloud optical thickness, and above-cloud integrated water vapor due to variations in aerosol sources, sea surface temperature, and large-scale subsidence patterns. The limited spatial extent also restricted our application to EMIT measurements, as we focused on the same geographic region to ensure the applicability of our a priori statistics. This constraint limited us to 3695 coincident observations between EMIT and the instruments aboard Aqua that met our constraints for cloud optical thickness and horizontal heterogeneity. Future work should incorporate in situ measurements from multiple field campaigns spanning diverse geographic regions and cloud regimes to develop more robust and generalizable a priori statistics, enabling a priori covariance matrices for different cloud types or meteorological conditions.

Our assumption of a smooth, monotonic adiabatic droplet profile does not capture the full complexity of real cloud microphysics. Figure 4 showed that in situ measurements exhibit rapid fluctuations in effective radius throughout the cloud, while our retrieved profiles necessarily represent smoothed approximations. However, Table 3 demonstrated that this simplification still enables substantially more accurate ***LWP*** estimation (26.9% error) compared to the vertically homogeneous assumption implicit in standard TBLUT retrievals (45.2% error). The success of the Wood–Hartmann adjustment (21.1% error) suggests that even simple parameterizations of vertical structure substantially improve retrieval accuracy. Future work should investigate the retrieval of multiple droplet sizes along the vertical dimension, rather than just values at cloud top and bottom, to improve the accuracy of the liquid water path retrieval. Additionally, the use of machine learning methods to retrieve droplet profiles would remove the need for strict assumptions that were made in the forward model developed for this analysis, such as adiabatic droplet growth within the cloud and fixed cloud top height.

The implications of this work extend beyond improved cloud property retrievals. Vertical profiles of droplet size provide insight into cloud droplet growth processes, the presence of drizzle, and the mixing of cloud top with dry air above [7–9]. More accurate liquid water path estimates are essential for constraining cloud albedo [10]. The ability to simultaneously retrieve above-cloud integrated water vapor may enable new investigations into the relationship between column integrated water vapor concentration and cloud droplet size. Future retrievals that estimate droplet size at more than just two heights within the cloud could be used to investigate the role of entrainment in modulating cloud albedo and lifetime. Looking toward future missions, the CLARREO Pathfinder HySICS instrument will provide unprecedented radiometric accuracy (0.3%) combined with contiguous spectral sampling from 350 to 2300 nm. Our results using simulated HySICS reflectance demonstrate that this combination of high accuracy and spectral resolution should enable routine retrieval of vertical cloud droplet profiles.

Author Contributions: Conceptualization, A.J.B. and P.P.; methodology, A.J.B.; software, A.J.B.; formal analysis, A.J.B.; investigation, A.J.B.; data curation, A.J.B.; writing—original draft preparation, A.J.B.; writing—review and editing, A.J.B. and P.P.; visualization, A.J.B.; supervision, P.P. All authors have read and agreed to the published version of the manuscript.

Funding: This material is based upon work supported by the National Science Foundation Graduate Research Fellowship under Grant No. 2040434 and NASA Contract Number 80LARC18C0001. Alpine is jointly funded by the University of Colorado Boulder, the University of Colorado Anschutz, and Colorado State University, and with support from NSF grants OAC-2201538 and OAC-2322260.

Data Availability Statement: The retrieval algorithm developed for this paper is freely available on GitHub (https://github.com/andrewjbuggee/GNOE-hyperspectral-retrieval.git, accessed on 23 July 2026). The MODIS L1B and geolocation files (https://doi.org/10.5067/MODIS/MYD021KM.061 and https://doi.org/10.5067/MODIS/MOD021KM.061, accessed on 13 August 2025), and the L2 files (https://doi.org/10.5067/MODIS/MOD06_L2.061 and https://doi.org/10.5067/MODIS/MYD06_L2.061, accessed on 13 August 2025) used for retrieving droplet profiles are freely available at NASA's Level-1 and Atmosphere Archive and Distribution System Distributed Active Archive Center (LAADS-DAAC), hosted at NASA's Goddard Space Flight Center (GSFC): https://ladsweb.modaps.eosdis.nasa.gov/, accessed on 23 July 2026. The VOCALS-REx data used for comparison with the multispectral retrievals are similarly defined within the GitHub repository. These data are maintained by the National Center for Atmospheric Research Earth Observing Laboratory Field Data Archive (NCAR EOL) and are freely available at: https://doi.org/10.5065/D60863M8, accessed on 1 March 2022. The AMSR-E/AMSR2 Unified L2B Global Swath Ocean Products (https://doi.org/10.5067/9YQRFKKEPUP4, accessed on 13 August 2025) used for verifying the retrieved products are freely available from the NASA National Snow and Ice Data Center Distributed Active Archive Center.

Acknowledgments: The authors would like to thank the team working on the LASICS tool for providing an early version of the code. We also want to thank the Instrument PI of CLARREO Pathfinder for discussions on the HySICS instrument and for providing the slit functions. Lastly, we would like to thank the EMIT team at JPL for discussing the EMIT noise model and calibration error with us. This work utilized the Alpine high-performance computing resource at the University of Colorado Boulder.

Conflicts of Interest: The authors declare no conflicts of interest. The funders had no role in the design of the study; in the collection, analyses, or interpretation of data; in the writing of the manuscript; or in the decision to publish the results.

Abbreviations

The following abbreviations are used in this manuscript:

MODIS	Moderate Resolution Imaging Spectroradiometer
EMIT	Earth Surface Mineral Dust Source Investigation
AMSR-E	Advanced Microwave Scanning Radiometer for EOS
AIRS	Atmospheric Infrared Sounder
VOCALS-REx	Variability of the American Monsoon Systems Ocean-Cloud-Atmosphere-Land Study Regional Experiment
CPF	CLARREO Pathfinder
HySICS	Hyperspectral imager for calibration science
TBLUT	Two-band look-up table
GNOE	Gauss–Newton Optimal Estimation

References

1. Wood, R. Stratus and Stratocumulus. *Encycl. Atmos. Sci.* **2015**, *2*, 196–200. [CrossRef]
2. L'Ecuyer, T.S.; Hang, Y.; Matus, A.V.; Wang, Z. Reassessing the Effect of Cloud Type on Earth's Energy Balance in the Age of Active Spaceborne Observations. Part I: Top of Atmosphere and Surface. *J. Clim.* **2019**, *32*, 6197–6217. [CrossRef]
3. Wood, R. Stratocumulus Clouds. *Mon. Weather Rev.* **2012**, *140*, 2373–2423. [CrossRef]
4. Miles, N.L.; Verlinde, J.; Clothiaux, E.E. Cloud Droplet Size Distributions in Low-Level Stratiform Clouds. *J. Atmos. Sci.* **2000**, *57*, 295–311. [CrossRef]

5. Meyer, K.; Platnick, S.; Arnold, G.T.; Amarasinghe, N.; Miller, D.; Small-Griswold, J.; Witte, M.; Cairns, B.; Gupta, S.; McFarquhar, G.; et al. Evaluating Spectral Cloud Effective Radius Retrievals from the Enhanced MODIS Airborne Simulator (eMAS) during ORACLES. *Atmos. Meas. Tech.* **2025**, *18*, 981–1011. [CrossRef]
6. Painemal, D.; Zuidema, P. Assessment of MODIS Cloud Effective Radius and Optical Thickness Retrievals over the Southeast Pacific with VOCALS-REx in Situ Measurements. *J. Geophys. Res. Atmos.* **2011**, *116*, D24206. [CrossRef]
7. Hill, A.A.; Feingold, G.; Jiang, H. The Influence of Entrainment and Mixing Assumption on Aerosol–Cloud Interactions in Marine Stratocumulus. *J. Atmos. Sci.* **2009**, *66*, 1450–1464. [CrossRef]
8. Magaritz-Ronen, L.; Pinsky, M.; Khain, A. Drizzle Formation in Stratocumulus Clouds: Effects of Turbulent Mixing. *Atmos. Chem. Phys.* **2016**, *16*, 1849–1862. [CrossRef]
9. Martins, J.V.; Marshak, A.; Remer, L.A.; Rosenfeld, D.; Kaufman, Y.J.; Fernandez-Borda, R.; Koren, I.; Correia, A.L.; Zubko, V.; Artaxo, P. Remote Sensing the Vertical Profile of Cloud Droplet Effective Radius, Thermodynamic Phase, and Temperature. *Atmos. Chem. Phys.* **2011**, *11*, 9485–9501. [CrossRef]
10. Borg, L.A.; Bennartz, R. Vertical Structure of Stratiform Marine Boundary Layer Clouds and Its Impact on Cloud Albedo. *Geophys. Res. Lett.* **2007**, *34*, L05807. [CrossRef]
11. Seethala, C.; Horváth, Á. Global Assessment of AMSR-E and MODIS Cloud Liquid Water Path Retrievals in Warm Oceanic Clouds. *J. Geophys. Res. Atmos.* **2010**, *115*, D13202. [CrossRef]
12. Miller, D.J.; Zhang, Z.; Ackerman, A.S.; Platnick, S.; Baum, B.A. The Impact of Cloud Vertical Profile on Liquid Water Path Retrieval Based on the Bispectral Method: A Theoretical Study Based on Large-eddy Simulations of Shallow Marine Boundary Layer Clouds. *J. Geophys. Res. Atmos.* **2016**, *121*, 4122–4141. [CrossRef] [PubMed]
13. Stephens, G.L.; Christensen, M.; Andrews, T.; Haywood, J.; Malavelle, F.F.; Suzuki, K.; Jing, X.; Lebsock, M.; Li, J.L.F.; Takahashi, H.; et al. Cloud Physics from Space. *Q. J. R. Meteorol. Soc.* **2019**, *145*, 2854–2875. [CrossRef]
14. Twomey, S.; Seton, K.J. Inferences of Gross Microphysical Properties of Clouds from Spectral Reflectance Measurements. *J. Atmos. Sci.* **1980**, *37*, 1065–1069. [CrossRef]
15. Nakajima, T.; King, M.D. Determination of the Optical Thickness and Effective Particle Radius of Clouds from Reflected Solar Radiation Measurements. Part I: Theory. *J. Atmos. Sci.* **1990**, *47*, 1878–1893. [CrossRef]
16. Twomey, S.; Bohren, C.F. Simple Approximations for Calculations of Absorption in Clouds. *J. Atmos. Sci.* **1980**, *37*, 2086–2094. [CrossRef]
17. Amarasinghe, N.; Platnick, S.; Meyer, K. Overview of the MODIS Collection 6 Cloud Optical Property (MOD06) Retrieval Look-up Tables. 2017. Available online: https://www.google.com/url?sa=t&source=web&rct=j&opi=89978449&url=https://atmosphere-imager.gsfc.nasa.gov/sites/default/files/ModAtmo/C6_LUT_document_final.pdf&ved=2ahUKEwiXpYae1-yVAxVrdfUHHe3RNfcQFnoECBoQAQ&usg=AOvVaw1OPJM2hXA7wmW0zd43Gq0E (accessed on 1 March 2023).
18. King, M.D.; Platnick, S.; Menzel, W.P.; Ackerman, S.A.; Hubanks, P.A. Spatial and Temporal Distribution of Clouds Observed by MODIS Onboard the Terra and Aqua Satellites. *IEEE Trans. Geosci. Remote Sens.* **2013**, *51*, 3826–3852. [CrossRef]
19. Platnick, S. Vertical Photon Transport in Cloud Remote Sensing Problems. *J. Geophys. Res. Atmos.* **2000**, *105*, 22919–22935. [CrossRef]
20. Buggee, A.J.; Pilewskie, P. Retrieving Vertical Profiles of Cloud Droplet Effective Radius Using Multispectral Measurements from MODIS: Examples and Limitations. *Atmos. Meas. Tech.* **2025**, *18*, 5299–5320. [CrossRef]
21. Chang, F.L.; Li, Z. Estimating the Vertical Variation of Cloud Droplet Effective Radius Using Multispectral Near-Infrared Satellite Measurements. *J. Geophys. Res. Atmos.* **2002**, *107*, AAC 7-1–AAC 7-12. [CrossRef]
22. Kokhanovsky, A.; Rozanov, V.V. Droplet Vertical Sizing in Warm Clouds Using Passive Optical Measurements from a Satellite. *Atmos. Meas. Tech.* **2012**, *5*, 517–528. [CrossRef]
23. King, N.J.; Vaughan, G. Using Passive Remote Sensing to Retrieve the Vertical Variation of Cloud Droplet Size in Marine Stratocumulus: An Assessment of Information Content and the Potential for Improved Retrievals from Hyperspectral Measurements. *J. Geophys. Res. Atmos.* **2012**, *117*, D15206. [CrossRef]
24. Shang, H.; Hioki, S.; Penide, G.; Cornet, C.; Letu, H.; Riedi, J. Establishment of an Analytical Model for Remote Sensing of Typical Stratocumulus Cloud Profiles under Various Precipitation and Entrainment Conditions. *Atmos. Chem. Phys.* **2023**, *23*, 2729–2746. [CrossRef]
25. Thompson, D.R.; Green, R.O.; Bradley, C.; Brodrick, P.G.; Mahowald, N.; Dor, E.B.; Bennett, M.; Bernas, M.; Carmon, N.; Chadwick, K.D.; et al. On-Orbit Calibration and Performance of the EMIT Imaging Spectrometer. *Remote Sens. Environ.* **2024**, *303*, 113986. [CrossRef]
26. Mero, B.; Lake, K.; Upcott-Gill, A.; Edwards, A.; Herrington, M.; Coste, P.; Binter, F.; Lopez, S.; Fournier, S.; Ballester, M.; et al. Status of the Design, Accommodation, and Performance of the TRUTHS Hyperspectral Imager at the End of Phase B1. In *Proceedings of the International Conference on Space Optics—ICSO 2022*; SPIE: Bellingham, WA, USA, 2023; Volume 12777, pp. 258–266.

27. Nieke, J.; Despoisse, L.; Gabriele, A.; Weber, H.; Strese, H.; Ghasemi, N.; Gascon, F.; Alonso, K.; Boccia, V.; Tsonevska, B.; et al. The Copernicus Hyperspectral Imaging Mission for the Environment (CHIME): An Overview of Its Mission, System and Planning Status. In *Proceedings of the Sensors, Systems, and Next-Generation Satellites XXVII*; SPIE: Bellingham, WA, USA, 2023; Volume 12729, pp. 21–40.
28. Shea, Y.; Fleming, G.; Kopp, G.; Lukashin, C.; Pilewskie, P.; Smith, P.; Thome, K.; Wielicki, B.; Liu, X.; Wu, W. Clarreo Pathfinder: Mission Overview and Current Status. *Int. Geosci. Remote Sens. Symp. (IGARSS)* **2020**, *4*, 3286–3289. [CrossRef]
29. Coddington, O.; Pilewskie, P.; Vukicevic, T. The Shannon Information Content of Hyperspectral Shortwave Cloud Albedo Measurements: Quantification and Practical Applications. *J. Geophys. Res. Atmos.* **2012**, *117*, D04205. [CrossRef]
30. Kopp, G.; Smith, P.; Belting, C.; Castleman, Z.; Drake, G.; Espejo, J.; Heuerman, K.; Lanzi, J.; Stuchlik, D. Radiometric Flight Results from the HyperSpectral Imager for Climate Science (HySICS). *Geosci. Instrum. Methods Data Syst.* **2017**, *6*, 169–191. [CrossRef]
31. Wood, R.; Mechoso, C.R.; Bretherton, C.S.; Weller, R.A.; Huebert, B.; Straneo, F.; Albrecht, B.A.; Coe, H.; Allen, G.; Vaughan, G.; et al. The VAMOS Ocean-Cloud-Atmosphere-Land Study Regional Experiment (VOCALS-REx): Goals, Platforms, and Field Operations. *Atmos. Chem. Phys.* **2011**, *11*, 627–654. [CrossRef]
32. Dubovik, O.; Fuertes, D.; Litvinov, P.; Lopatin, A.; Lapyonok, T.; Doubovik, I.; Xu, F.; Ducos, F.; Chen, C.; Torres, B.; et al. A Comprehensive Description of Multi-Term LSM for Applying Multiple a Priori Constraints in Problems of Atmospheric Remote Sensing: GRASP Algorithm, Concept, and Applications. *Front. Remote Sens.* **2021**, *2*, 706851. [CrossRef]
33. Maahn, M.; Turner, D.D.; Löhnert, U.; Posselt, D.J.; Ebell, K.; Mace, G.G.; Comstock, J.M. Optimal Estimation Retrievals and Their Uncertainties: What Every Atmospheric Scientist Should Know. *Bull. Am. Meteor. Soc.* **2020**, *101*, E1512–E1523. [CrossRef]
34. Green, R.O.; Mahowald, N.; Ung, C.; Thompson, D.R.; Bator, L.; Bennet, M.; Bernas, M.; Blackway, N.; Bradley, C.; Cha, J.; et al. The Earth Surface Mineral Dust Source Investigation: An Earth Science Imaging Spectroscopy Mission. In *Proceedings of the 2020 IEEE Aerospace Conference, Big Sky, MT, USA, 7–14 March 2020*; IEEE: Piscataway, NJ, USA, 2020; pp. 1–15.
35. Rodgers, C.D. *Inverse Methods for Atmospheric Souding: Theory and Practice*; World Scientific: Singapore, 2000; Volume 2.
36. Poulsen, C.A.; Siddans, R.; Thomas, G.E.; Sayer, A.M.; Grainger, R.G.; Campmany, E.; Dean, S.M.; Arnold, C.; Watts, P.D. Cloud Retrievals from Satellite Data Using Optimal Estimation: Evaluation and Application to ATSR. *Atmos. Meas. Tech.* **2012**, *5*, 1889–1910. [CrossRef]
37. Doicu, A.; Schreier, F.; Hess, M. Iteratively Regularized Gauss–Newton Method for Bound-Constraint Problems in Atmospheric Remote Sensing. *Comput. Phys. Commun.* **2003**, *153*, 59–65. [CrossRef]
38. Emde, C.; Buras-Schnell, R.; Kylling, A.; Mayer, B.; Gasteiger, J.; Hamann, U.; Kylling, J.; Richter, B.; Pause, C.; Dowling, T.; et al. The libRadtran Software Package for Radiative Transfer Calculations (Version 2.0.1). *Geosci. Model Dev.* **2016**, *9*, 1647–1672. [CrossRef]
39. Stamnes, K.; Tsay, S.-C.; Wiscombe, W.; Laszlo, I. DISORT, a General-Purpose Fortran Program for Discrete-Ordinate-Method Radiative Transfer in Scattering and Emitting Layered Media: Documentation of Methodology. 2000. Available online: https://web.gps.caltech.edu/ vijay/Papers/RT%20Models/DISORT%20Report.pdf (accessed on 2 March 2023).
40. Coddington, O.M.; Richard, E.C.; Harber, D.; Pilewskie, P.; Woods, T.N.; Snow, M.; Chance, K.; Liu, X.; Sun, K. Version 2 of the TSIS-1 Hybrid Solar Reference Spectrum and Extension to the Full Spectrum. *Earth Space Sci.* **2023**, *10*, e2022EA002637. [CrossRef]
41. Hersbach, H.; Bell, B.; Berrisford, P.; Hirahara, S.; Horányi, A.; Muñoz-Sabater, J.; Nicolas, J.; Peubey, C.; Radu, R.; Schepers, D.; et al. The ERA5 Global Reanalysis. *Q. J. R. Meteorol. Soc.* **2020**, *146*, 1999–2049. [CrossRef]
42. Cox, C.; Munk, W. Measurement of the Roughness of the Sea Surface from Photographs of the Sun's Glitter. *J. Opt. Soc. Am. JOSA* **1954**, *44*, 838–850. [CrossRef]
43. Anderson, G.P.; Chetwynd, J.H.; Clough, S.A.; She1tle, E.P.; Kneizys, F.X. *AFGL Atmospheric Constituent Profiles (0–120 km)*; AFGL-TR-86-0110; Optical Physics Division, Air Force Geophysics Laboratory: Bedford, MA, USA, 1986.
44. Minnis, P.; Sun-Mack, S.; Young, D.F.; Heck, P.W.; Garber, D.P.; Chen, Y.; Spangenberg, D.A.; Arduini, R.F.; Trepte, Q.Z.; Smith, W.L.; et al. CERES Edition-2 Cloud Property Retrievals Using TRMM VIRS and Terra and Aqua MODIS Data—Part I: Algorithms. *IEEE Trans. Geosci. Remote Sens.* **2011**, *49*, 4374–4400. [CrossRef]
45. Platnick, S.; King, M.D.; Ackerman, S.A.; Menzel, W.P.; Baum, B.A.; Riédi, J.C.; Frey, R.A. The MODIS Cloud Products: Algorithms and Examples from Terra. *IEEE Trans. Geosci. Remote Sens.* **2003**, *41*, 459–472. [CrossRef]
46. Sayer, A.M.; Poulsen, C.A.; Arnold, C.; Campmany, E.; Dean, S.; Ewen, G.B.L.; Grainger, R.G.; Lawrence, B.N.; Siddans, R.; Thomas, G.E.; et al. Global Retrieval of ATSR Cloud Parameters and Evaluation (GRAPE): Dataset Assessment. *Atmos. Chem. Phys.* **2011**, *11*, 3913–3936. [CrossRef]
47. Albert, P.; Bennartz, R.; Fischer, J. Remote Sensing of Atmospheric Water Vapor from Backscattered Sunlight in Cloudy Atmospheres. *J. Atmos. Ocean. Technol.* **2001**, *18*, 865–874. [CrossRef]

48. Rodgers, C.D. Information Content and Optimization of High-Spectral-Resolution Measurements. *Opt. Spectrosc. Tech. Instrum. Atmos. Space Res. II* **1996**, *2830*, 136. [CrossRef]
49. Dubovik, O.; King, M.D. A Flexible Inversion Algorithm for Retrieval of Aerosol Optical Properties from Sun and Sky Radiance Measurements. *J. Geophys. Res. Atmos.* **2000**, *105*, 20673–20696. [CrossRef]
50. Wilks, D.S. *Statistical Methods in the Atmospheric Sciences*, 3rd ed.; International geophysics series; Elsevier/Academic Press: Amsterdam, The Netherlands; Boston, MA, USA, 2011; ISBN 978-0-12-385022-5.
51. Lance, S.; Brock, C.A.; Rogers, D.; Gordon, J.A. Water Droplet Calibration of the Cloud Droplet Probe (CDP) and in-Flight Performance in Liquid, Ice and Mixed-Phase Clouds during ARCPAC. *Atmos. Meas. Tech.* **2010**, *3*, 1683–1706. [CrossRef]
52. Platnick, S.; Meyer, K.G.; King, M.D.; Wind, G.; Amarasinghe, N.; Marchant, B.; Arnold, G.T.; Zhang, Z.; Hubanks, P.A.; Holz, R.E.; et al. The MODIS Cloud Optical and Microphysical Products: Collection 6 Updates and Examples from Terra and Aqua. *IEEE Trans. Geosci. Remote Sens.* **2017**, *55*, 502–525. [CrossRef] [PubMed]
53. Painemal, D.; Kato, S.; Minnis, P. Boundary Layer Regulation in the Southeast Atlantic Cloud Microphysics during the Biomass Burning Season as Seen by the A-Train Satellite Constellation. *J. Geophys. Res. Atmos.* **2014**, *119*, 11288–11302. [CrossRef]
54. Gopalan, A.; Shea, Y.; Siman-tov, E.; Roithmayr, C.; Doelling, D.R.; Scarino, B.R. Langley Automated Sensor Inter-Calibration System (LASICS): Open Access Tools for Satellite Imager Inter-Calibration. Presented at the AMS 101st Annual Meeting, Virtual, 10–15 January 2021.
55. Gao, B.-C.; Kaufman, Y.J. *The MODIS Near-IR Water Vapor Algorithm*; TBD-MOD-03; NASA: Washington, DC, USA, 1998.
56. Duncan, D.I.; Kummerow, C.D. A 1DVAR Retrieval Applied to GMI: Algorithm Description, Validation, and Sensitivities. *J. Geophys. Res. Atmos.* **2016**, *121*, 7415–7429. [CrossRef]
57. Kummerow, C.; Ferraro, R.; Duncan, D. *AMSR-E/AMSR2 Unified L2B Global Swath Ocean Products, Version 1: User Guide*; NASA National Snow and Ice Data Center: Boulder, CO, USA, 2021.
58. Greenwald, T.J. A 2 Year Comparison of AMSR-E and MODIS Cloud Liquid Water Path Observations. *Geophys. Res. Lett.* **2009**, *36*, L20805. [CrossRef]
59. Liu, C.-C.; Zhu, Y.; Wang, L.; Bardeen, C.; Maloney, C.; Tilmes, S.; Vitt, F.; Kay, J.E.; Herrington, A.R.; Larson, V.E.; et al. Performance and Evaluation of a Sectional Cloud Microphysical Model (CARMA Cloud) in the Community Earth System Model (CESM2). 2026. Available online: https://essopenarchive.org/doi/full/10.22541/essoar.176824045.59749413 (accessed on 20 March 2026).
60. Duncan, D.I.; Kummerow, C.D.; Meier, W.N. An Integrated Examination of AMSR2 Products Over Ocean. *IEEE J. Sel. Top. Appl. Earth Obs. Remote Sens.* **2017**, *10*, 3963–3974. [CrossRef]
61. Strow, L.L.; Hannon, S.E.; Weiler, M.; Overoye, K.; Gaiser, S.L.; Aumann, H.H. Prelaunch Spectral Calibration of the Atmospheric Infrared Sounder (AIRS). *IEEE Trans. Geosci. Remote Sens.* **2003**, *41*, 274–286. [CrossRef]
62. Maning, E.; Kahn, B.; Fetzer, E.J.; Yue, Q.; Wong, S.; Kalmus, P.; Payne, V.; Wong, T.; Olsen, E.T.; Wilson, R.C.; et al. *AIRS/AMSU/HSB Version 7 Level 2 Product User Guide*; Jet Propulsion Laboratory: Pasadena, CA, USA, 2021; p. 197.
63. Zhang, Z.; Platnick, S. An Assessment of Differences between Cloud Effective Particle Radius Retrievals for Marine Water Clouds from Three MODIS Spectral Bands. *J. Geophys. Res.* **2011**, *116*, D20215. [CrossRef]
64. Feingold, G.; Furrer, R.; Pilewskie, P.; Remer, L.A.; Min, Q.; Jonsson, H. Aerosol Indirect Effect Studies at Southern Great Plains during the May 2003 Intensive Operations Period. *J. Geophys. Res. Atmos.* **2006**, *111*, D05S14. [CrossRef]
65. Thompson, D.R.; Green, R.O. *EMIT L1B Algorithm Theoretical Basis: Calibrated Radiance at Sensor*; JPL D-104254 L1B; ATBD-EMIT-01; Jet Propulsion Laboratory, California Institute of Technology: Pasadena, CA, USA, 2020.
66. Coleman, R.W.; Thompson, D.R.; Brodrick, P.G.; Dor, E.B.; Cox, E.; Pérez García-Pando, C.; Hoefen, T.; Kokaly, R.F.; Meyer, J.M.; Ochoa, F.; et al. An Accuracy Assessment of the Surface Reflectance Product from the EMIT Imaging Spectrometer. *Remote Sens. Environ.* **2024**, *315*, 114450. [CrossRef]
67. Wood, R.; Hartmann, D.L. Spatial Variability of Liquid Water Path in Marine Low Cloud: The Importance of Mesoscale Cellular Convection. *J. Clim.* **2006**, *19*, 1748–1764. [CrossRef]
68. Platnick, S.; Meyer, K.G.; King, M.D.; Wind, G.; Amarasinghe, N.; Marchant, B.; Thomas Arnold, G.; Zhang, Z.; Hubanks, P.A.; Ridgway, B.; et al. *MODIS Cloud Optical Properties: User Guide for the Collection 6/6.1 Level-2 MOD06/MYD06 Product and Associated Level-3 Datasets*; NASA: Washington, DC, USA, 2018.
69. Chen, R.; Chang, F.-L.; Li, Z.; Ferraro, R.; Weng, F. Impact of the Vertical Variation of Cloud Droplet Size on the Estimation of Cloud Liquid Water Path and Rain Detection. *J. Atmos. Sci.* **2007**, *64*, 3843–3853. [CrossRef]
70. Chang, F.-L.; Li, Z. Retrieving Vertical Profiles of Water-Cloud Droplet Effective Radius: Algorithm Modification and Preliminary Application. *J. Geophys. Res. Atmos.* **2003**, *108*, 4763. [CrossRef]

71. Susskind, J.; Barnet, C.D.; Blaisdell, J.M. Retrieval of Atmospheric and Surface Parameters from AIRS/AMSU/HSB Data in the Presence of Clouds. *IEEE Trans. Geosci. Remote Sens.* **2003**, *41*, 390–409. [CrossRef]
72. Zhang, Z.; Ackerman, A.S.; Feingold, G.; Platnick, S.; Pincus, R.; Xue, H. Effects of Cloud Horizontal Inhomogeneity and Drizzle on Remote Sensing of Cloud Droplet Effective Radius: Case Studies Based on Large-Eddy Simulations. *J. Geophys. Res. Atmos.* **2012**, *117*, D19208. [CrossRef]

Disclaimer/Publisher's Note: The statements, opinions and data contained in all publications are solely those of the individual author(s) and contributor(s) and not of MDPI and/or the editor(s). MDPI and/or the editor(s) disclaim responsibility for any injury to people or property resulting from any ideas, methods, instructions or products referred to in the content.